

9270

NACA TN 2957



NATIONAL ADVISORY COMMITTEE FOR AERONAUTICS

TECHNICAL NOTE 2957

SURVEYS OF THE FLOW FIELDS AT THE PROPELLER PLANES
OF SIX 40° SWEEPBACK WING-FUSELAGE-
NACELLE COMBINATIONS

By Vernon L. Rogallo and John L. McCloud III

Ames Aeronautical Laboratory
Moffett Field, Calif.



Washington

June 1953

AFMCC
TECHNICAL LIBRARY

AFL 2811



TECHNICAL NOTE 2957

SURVEYS OF THE FLOW FIELDS AT THE PROPELLER PLANES
OF SIX 40° SWEEPBACK WING-FUSELAGE-
NACELLE COMBINATIONS

By Vernon L. Rogallo and John L. McCloud III

SUMMARY

The flow fields at the propeller planes of six 40° sweptback semi-span wing-fuselage-nacelle combinations were surveyed to provide data to enable the study of the characteristics of the flow fields and their effect on propeller-oscillating aerodynamic loads. The results of the surveys are presented in the form of angles that define the direction of the local velocity relative to the survey disk and as the ratios of the local velocities to free-stream velocity. These parameters are shown as functions of the angular position around the survey disk for given radial positions. Typical propeller-oscillating air loads, computed by the method of NACA TN 2192 using measured flow-field data, are presented to demonstrate the significance of the flow parameters. Also shown are comparisons of measured and predicted upflow angles for all models at a specific angle of attack.

The results of the surveys show that variations of the flow parameters with angular position are predominantly first-order sinusoidal for the six models tested and, thus, are similar to results for an unswept-wing airplane reported in NACA TN 2192.

The rotational flow angle is the major contributor to the oscillating aerodynamic loads and has its maximum and minimum values at the horizontal center line of the propeller disk, where its value is determined by the upflow angle.

The upflow angles predicted by the methods of NACA TN's 2795 and 2894 were found to be in good agreement with measured angles.

INTRODUCTION

Vibratory stresses are introduced in propeller blades by oscillating aerodynamic loads which result from rotation of the propeller (inclined

or noninclined) in a nonuniform flow field¹ (see ref. 1). A detailed study of the air flow at the propeller planes of a twin-engine airplane with an unswept wing was reported in reference 2, and it was demonstrated therein that the upflow angle (sum of upwash and geometric angles) at the horizontal center line of the propeller disk was the major contributor to the propeller-oscillating aerodynamic loads. A method for predicting the upwash components of the total upflow angles at the horizontal center line of propeller disks for airplanes with unswept wings is presented in reference 3, and experimental verification is given therein.

The method of reference 3 was extended in references 4 and 5 for application to airplanes having wings of arbitrary plan form with nacelles at arbitrary vertical locations. Limited experimental upflow data which substantiate the method for the swept-wing case are presented in reference 5 for several nacelle locations.

More complete experimental data for the case of the swept-wing airplane are needed to determine the significance of the flow-field parameters which determine the oscillating aerodynamic loads and, also, the extent to which these loads are dependent on the upflow angles at the horizontal center lines of the propeller disks. Presented herein are the results of detailed flow measurements at the propeller planes of six 40° sweptback, semispan wing-fuselage-nacelle combinations which differ in aspect ratio, taper ratio, and nacelle location and inclination. Typical oscillating air loads, computed by the method of reference 2 using measured flow-field data, are presented in order to demonstrate the significance of the flow-field parameters. In addition, the measured and predicted upflow angles together with the predicted upwash components are presented for each model.

NOTATION

A	total upflow angle, angle between the propeller thrust axis and the direction of the local flow, ² $\alpha_G + \epsilon$, deg
b	span of wing measured perpendicular to the vertical plane of symmetry, ft
C_L	lift coefficient, $\frac{\text{total lift}}{qS}$
c	local chord of the wing at the inboard nacelle, ² ft

¹Oscillating air loads may also be introduced by rotating a propeller inclined in a uniform flow field.

²Measured in a plane parallel to the model plane of symmetry.

c_t	section thrust coefficient, $\frac{\text{section thrust}}{\rho n^2 D^4}$
Δc_t	incremental section thrust coefficient, $c_{t\Omega} - c_{t\Omega = 0}$
D	propeller diameter, ft
L	body length, ft
M	free-stream Mach number
n	propeller speed, rps
q	free-stream dynamic pressure, $\rho V_0^2/2$, lb/sq ft
r	distance along any radial line from propeller thrust axis, ft
S	wing area, sq ft
V_0	free-stream velocity, ft/sec
V_l	local velocity at any point (r, Ω) at the survey disk, ft/sec (Direction of this velocity is defined by the angles θ and ψ . See fig. 1.)
V_l/V_0	velocity ratio at any point (r, Ω) at the survey disk
v'	component of the local velocity in the plane perpendicular to a radial line, ft/sec
y	distance from model plane of symmetry, ft
α_G	angle between the propeller thrust axis and the direction of free-stream velocity, ² deg (See fig. 1.)
α_w	angle between wing-root chord and direction of free stream, ² deg
γ	propeller thrust-axis inclination as measured from the wing-root chord (negative below wing-chord line), ² deg
ϵ	angle of upwash ² measured from the free-stream direction, deg
η	dimensionless lateral coordinate, semispans
θ	angle of outflow, measured from a line parallel to the propeller thrust axis in a plane through the propeller thrust axis, deg (See fig. 1.)

²See footnote 2, p. 2.

θ'	angle at which the local velocity at any point on the survey disk is inclined to the plane perpendicular to the radial line through that point, deg (See fig. 1.)
Λ	sweep of the wing quarter-chord line, positive for sweepback, deg
λ	wing taper ratio, $\frac{\text{tip chord}}{\text{root chord}}$
ρ	mass density of air in free stream, slugs/cu ft
r	dimensionless longitudinal coordinate, distance ahead of wing quarter-chord line, ² semispans
ψ	angle of rotational flow (an apparent, not an actual rotation), measured from a line parallel to the propeller thrust axis in a plane perpendicular to a radial line, deg (See fig. 1.)
Ω	angular position about the propeller thrust axis, measured counterclockwise from the upper vertical position as seen from the front, deg (See fig. 1.)

MODELS AND APPARATUS

The six semispan-model, 40° sweptback wing-fuselage-nacelle combinations used in this investigation are shown in figure 2, together with pertinent information concerning each. The model designations indicated in figure 2 are used throughout this report. It may be noted that the most important differences between models are the chordwise and vertical locations and inclination of the longitudinal axis of the nacelles.³ Photographs of models B, D, and E mounted in the Ames 40- by 80-foot wind tunnel are shown in figure 3. The various model configurations have been made by modification of a basic model, the general arrangement and pertinent dimensions of which are shown in figure 4. The fuselage and nacelle coordinates are shown in figure 5.

The survey rake consisted of six directional pitot-static tubes mounted at various intervals along a steel tube. Details of the survey rake are shown in figure 6. The rake is shown mounted on the models in figure 3.

²See footnote 2, p. 2.

³The propeller thrust axes were assumed to be coincident with the nacelle longitudinal axes.

TEST CONDITIONS

The flow-field measurements and force tests were made in the Ames 40- by 80-foot wind tunnel at the following test conditions:

Dynamic pressure	25 lb/sq ft
Mach number	0.13
Reynolds number (based on wing M.A.C.)	
Models A and B	5,500,000
Models C, D, E, and F	5,800,000
Angle-of-attack range	-4° to 12°

RESULTS

The propeller flow field is best described by the variation of the flow parameters Ψ , θ , and V_L/V_O with angular position Ω around the disk for various radial distances r from the propeller axis. Since the load on a propeller blade at a given angular position is related to the flow parameters at that angular position, the variation of the flow parameters with angular position characterizes the oscillating air load. Typical variations of the flow parameters with angular position are presented in the following figures for all models:

Figure	Flow parameter	α_w	Radial station, ft
7	Rotational flow angle, Ψ	-4,0,4,8,12	3.89,2.56,1.23
8	Outflow angle, θ	-4,0,4,8,12	3.89,2.56,1.23
9	Velocity ratio, V_L/V_O	-4,0,4,8,12	3.89,2.56,1.23

Figures 10, 11, and 12 show the variation of the flow parameters with radial position along several diameters of the survey disk of the inboard nacelle of model B. These variations are typical of each model, and it is evident that the values at the radial stations 3.89, 2.56, and 1.23 adequately define these curves; therefore, cross plots of figures 7, 8, and 9 could be used for attaining the radial variation of the flow parameters for all models, if desired.

Figure 13 shows typical oscillating air loads for a propeller-blade element operating in the flow fields of several of the sweptback wing-fuselage-nacelle combinations. For each of the combinations, a comparison is shown of the oscillating air load computed using the complete flow-field data with that computed using only the rotational flow angles and assuming that

$$V_L/V_O \cos \theta' = 1$$

(This is tantamount to assuming $V_1/V_0 = 1$ and $\theta = 0^\circ$ for all Ω 's.) The method of reference 2 was used for these computations.

Measured and predicted upflow angles for all models are shown in figure 14. The predicted upwash angles shown in figure 14 (computed by the methods of refs. 4 and 5) are presented to facilitate the discussion of the effects of nacelle location and inclination.

Lift curves of the six models are shown in figure 15 for all models.

No corrections have been applied to the flow measurements or the lift curve, since the Ames 40- by 80-foot wind-tunnel-wall corrections are negligible for a semispan model of this size.

DISCUSSION

Propeller Flow Fields

From examination of figures 7, 8, and 9, it is seen that the variation of the flow parameters, ψ , θ , and V_1/V_0 , with angular position are predominantly first-order sinusoidal. The outflow angle and velocity ratio are approximately in phase with each other and 90° out of phase with the rotational flow angle. These characteristics are similar to those found for the unswept-wing airplane as reported in reference 2. For all models, the maximum and minimum values of ψ occur when Ω is approximately equal to 90° and 270° . These values of Ω establish the horizontal center line of the propeller disk for which

$$\psi_{90^\circ} = -(\alpha_G + \epsilon_{90^\circ}) = -A_{90^\circ}$$

$$\psi_{270^\circ} = +(\alpha_G + \epsilon_{270^\circ}) = +A_{270^\circ}$$

Oscillating Aerodynamic Loading

The oscillating air loads, as indicated by the variation of the thrust coefficient⁴ with angular position (shown in fig. 13), were computed by use of the entire flow-field data and by use of only the measured rotational flow angle, ψ . Also shown in figure 13 are the flow-field parameters used in the computations. Comparison of the loadings shows that ψ is the major contributor to the oscillating air load. For each model the magnitudes of the variations are not greatly different for the two cases; hence, the magnitude of the oscillating air load due to the complete flow field can be estimated with good accuracy if the maximum and minimum values of ψ are known.

⁴These thrust coefficients were computed by the method of reference 2.

On the basis of all the foregoing, the total upflow angles at the horizontal center line of the propeller disk provide a rational basis for comparison of the models with respect to the magnitude of the oscillating air load.

The Upflow Angles at the Horizontal Center Lines of the Propeller Disks

The measured and predicted upflow angles are shown in figure 14. A wing angle of attack of 10° was chosen for the comparisons as representative of a climbing attitude where the magnitude of the propeller vibratory stresses would be large. At this angle of attack, all models have approximately the same lift coefficient (see fig. 15). When comparing the models, it is important to consider both the level and asymmetry of the upflow. A high level of upflow is indicative of a large first-order component of the oscillating air load; the asymmetry of the upflow distribution is primarily associated with higher-order components of the oscillating air loads. The predicted upwash components will be used in explaining the differences in the upflow for the models because, as may be seen in figure 14, the agreement between the measured and predicted upflow angles was of the same order at various points along the horizontal center line of the propeller disks and for the different nacelle locations at a given angle of attack.

The effect of chordwise location of the propeller disks is shown in the upflow and upwash variations of models A and B (fig. 14). Model A, which has its nacelles (hence, propeller disks) farthest forward, has a somewhat lower level and a lesser amount of asymmetry of upflow than model B. However, these reductions are insignificant in that there would be no sizable differences in the oscillating air load of propellers located within the limits of the chordwise positions investigated.

The effects of spanwise location of the propeller disks (as associated with swept-wing airplanes) are apparent in the upflow and upwash variations of models A, B, C, and D. The magnitude and asymmetry of the upflow are somewhat greater at the outboard survey disks than at the inboard survey disk. Comparison of upflow and upwash characteristics at the inboard survey disk of model C with those at the survey disk of model D (model D has only an inboard nacelle) shows that the outboard nacelle of model C induces no significant upwash at the inboard survey disk.

The effect of vertical location of the nacelles is shown in the upflow and upwash characteristics of models D, E, and F (fig. 14). The pylon-mounted nacelles of models E and F have little or no asymmetry of upflow and a lower level of upflow than model D. These reductions are significant in that they indicate a sizable change in the oscillating

air load may be realized from changes in the vertical position of the horizontal center line of a propeller disk.

The effect of nacelle and thrust-axis inclination is shown in the upflow and upwash characteristics of model F which has considerably less nacelle-induced upwash than all other models. Although only a slight reduction in total upwash resulted from tilting the nacelle downward, the large reduction in the thrust-axis inclination considerably reduced the magnitude of the upflow angles. Since the rate of change of the upflow angle with angle of attack, $dA/d\alpha$, is independent of thrust-axis inclination,⁵ γ , minimum upflow angles at the horizontal center line of a propeller disk can only occur at a given angle of attack. A method is presented in Appendix B of reference 4 for selection of thrust- and nacelle-axis inclination for minimizing oscillating air loads.

CONCLUSIONS

From the results of surveys of the propeller flow fields of six 40° sweptback, semispan wing-fuselage-nacelle combinations, the following conclusions may be drawn:

1. Variations of the flow parameters with angular position are predominantly first-order sinusoidal for the six models tested and, thus, similar to results for an unswept-wing airplane reported in NACA TN 2192.
2. The rotational flow angle is the major contributor to the oscillating aerodynamic loads and has its maximum and minimum values at the horizontal center line of the propeller disk, where its value is determined by the thrust-axis angle of attack and the total upwash angle.
3. From the upflow characteristics of the models tested, it was found that significant reductions in the upflow angles were obtained by lowering the horizontal center line of the propeller disk.
4. The upflow angles predicted by the methods of NACA TN's 2795 and 2894 were found to be in good agreement with measured angles.

Ames Aeronautical Laboratory
National Advisory Committee for Aeronautics
Moffett Field, Calif., Mar. 31, 1953

⁵If a change in the position of the horizontal center line of the propeller disk results from inclination of the thrust axis, $dA/d\alpha$ may be altered.

REFERENCES

1. Rogallo, Vernon L., Roberts, John C., and Oldaker, Merritt R.: Vibratory Stresses in Propellers Operating in the Flow Field of a Wing-Nacelle-Fuselage Combination. NACA TN 2308, 1951.
2. Roberts, John C., and Yaggy, Paul F.: A Survey of the Flow at the Plane of the Propeller of a Twin-Engine Airplane. NACA TN 2192, 1950.
3. Yaggy, Paul F.: A Method for Predicting the Upwash Angles Induced at the Propeller Plane of a Combination of Bodies With an Unswept Wing. NACA TN 2528, 1951.
4. Rogallo, Vernon L.: Effects of Wing Sweep on the Upwash at the Propeller Planes of Multiengine Airplanes. NACA TN 2795, 1952.
5. Rogallo, Vernon L., and McCloud, John L., III: Calculations of Upwash in the Region Above or Below the Wing-Chord Planes of Swept-Back Wing-Fuselage-Nacelle Combinations. NACA TN 2894, 1953.

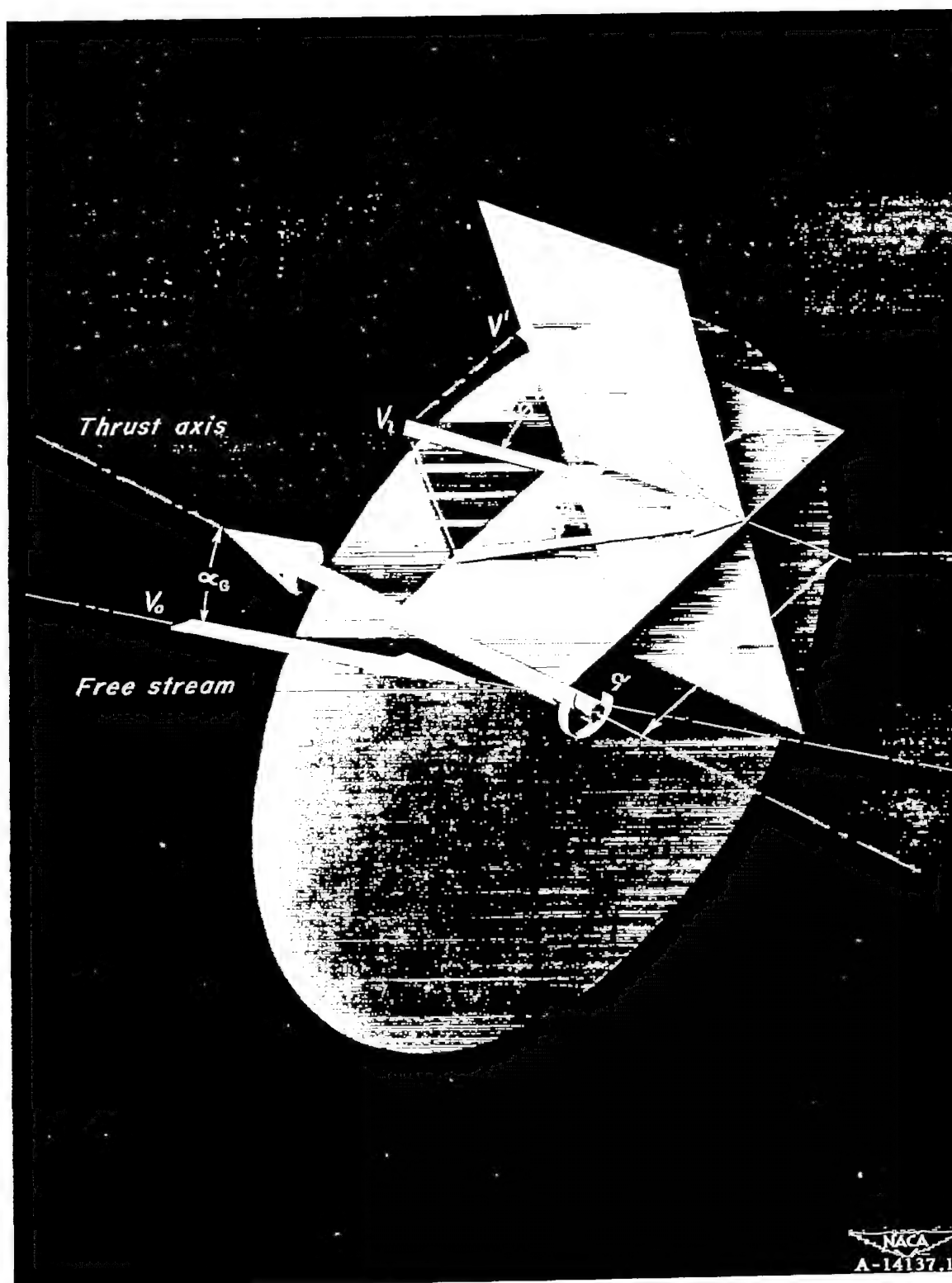
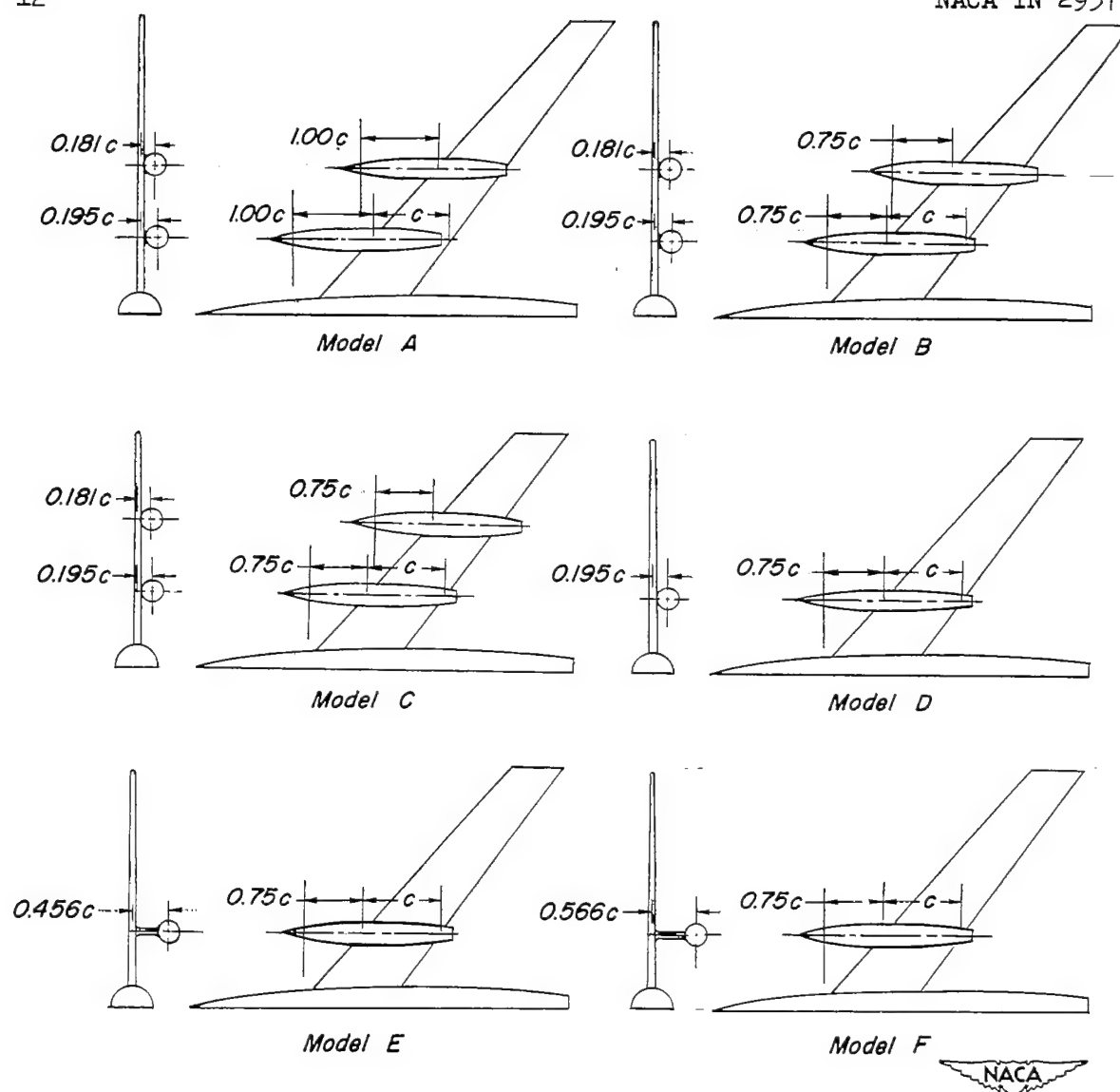


Figure 1.- Geometric characteristics of the flow parameters relative to the survey disk. All angles are shown positive.



Model	A	B	C	D	E	F
Aspect ratio	10	10	7.3	7.3	7.3	7.3
Nacelle location, η						
Inboard	0.25	0.25	0.31	0.31	0.31	0.31
Outboard	0.50	0.50	0.62	—	—	—
Taper ratio	0.34	0.34	0.49	0.49	0.49	0.49
Nacelle inclination	0°	0°	0°	0°	0°	-7°

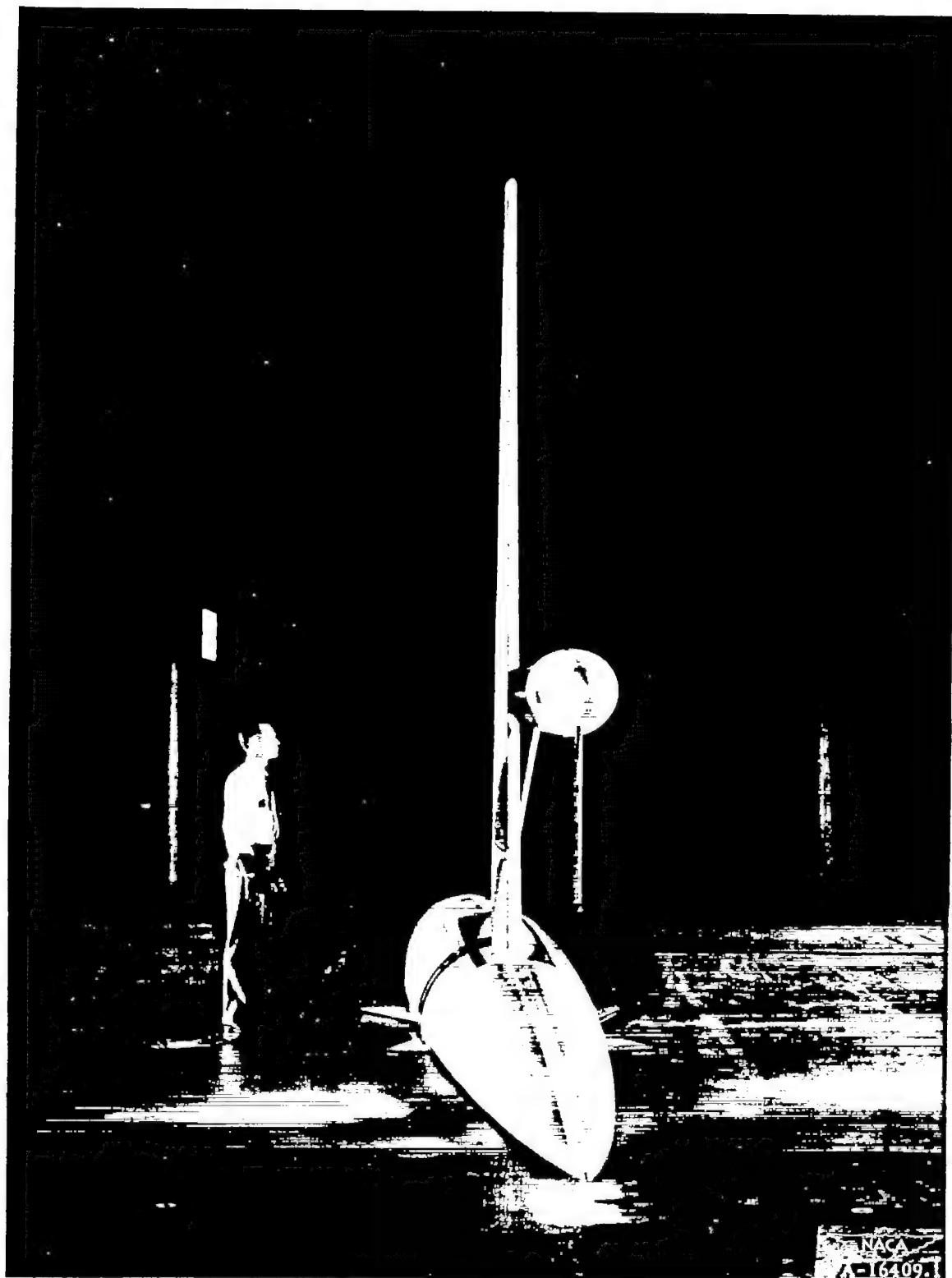
Note: Extent of survey from nacelle center line, 0.19c to 0.61c.

Figure 2. — Semispan models. Δ , 40°.



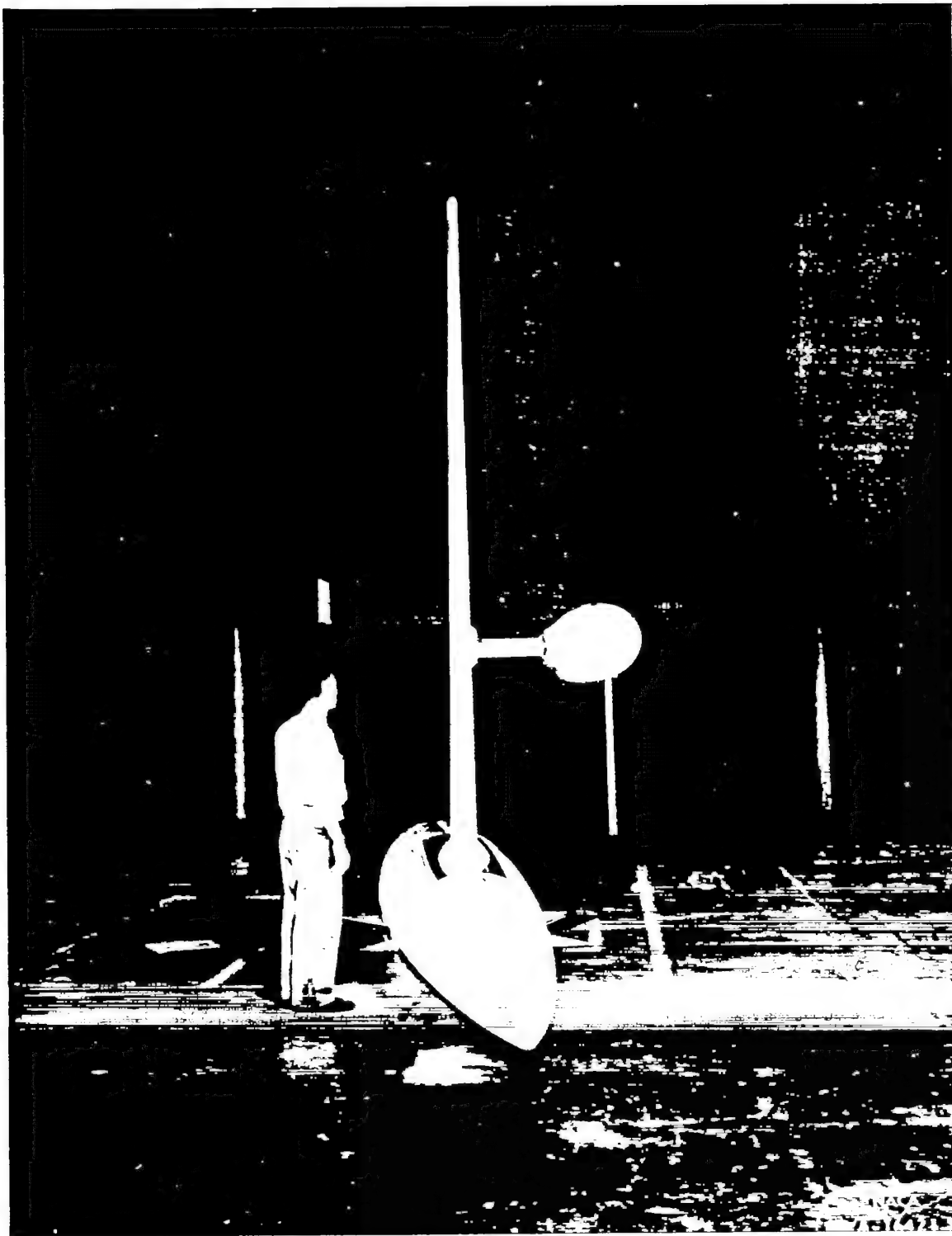
(a) Model B.

Figure 3.- The models mounted in the 40- by 80-foot wind tunnel.



(b) Model D.

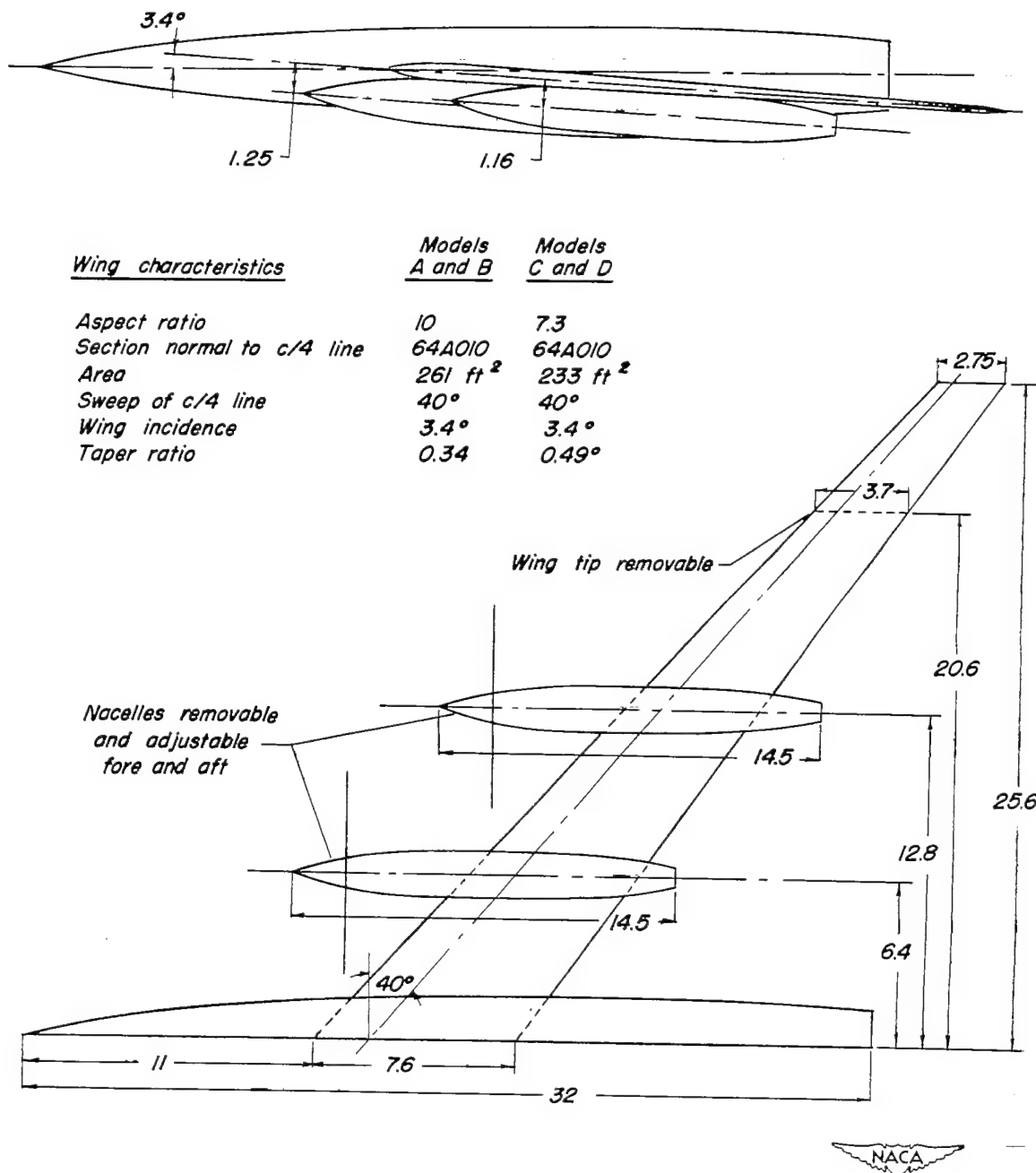
Figure 3.- Continued.



(c) Model E.

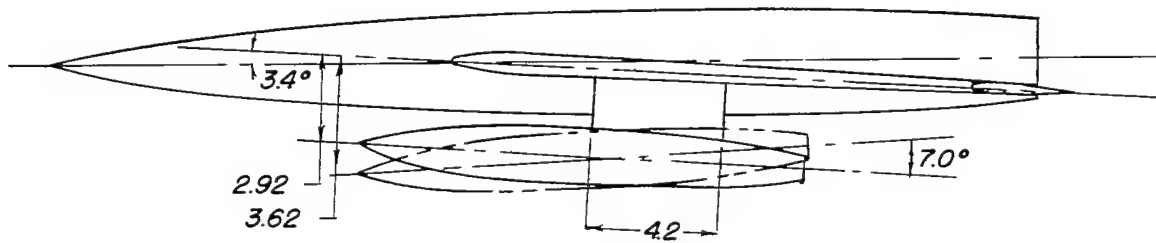
Figure 3.- Concluded.

All dimensions are in feet

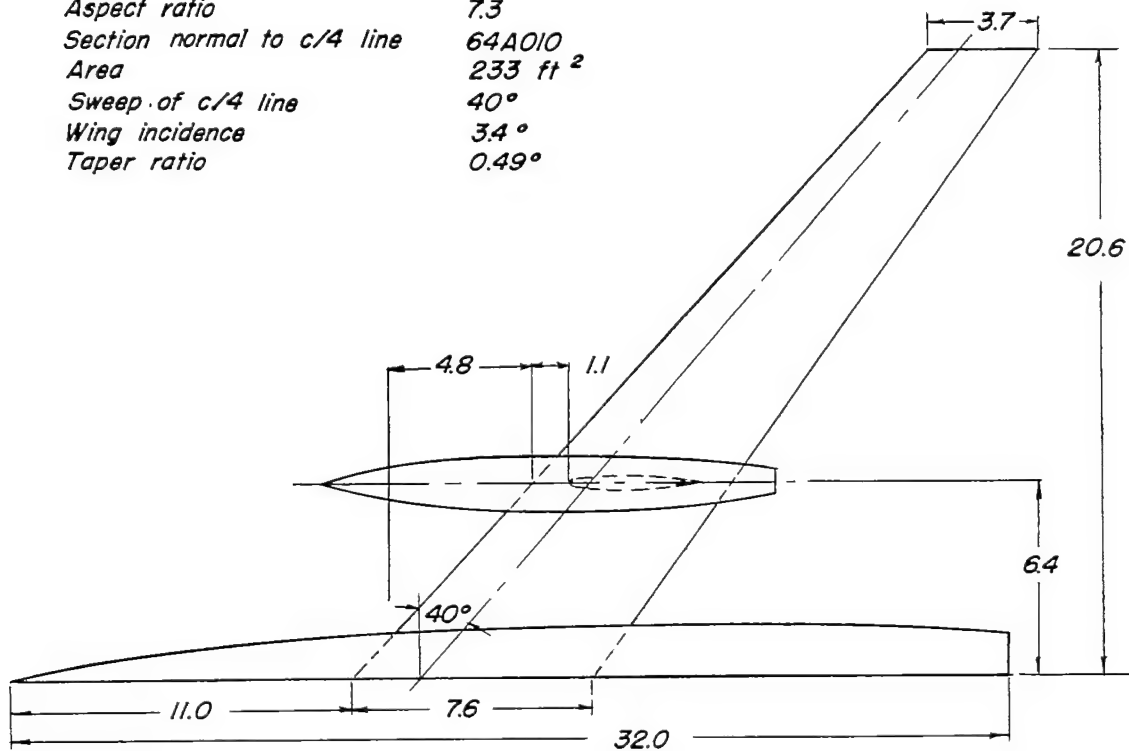


(a) Models A, B, C, and D.

Figure 4.— General arrangements and dimensions of test models.



<u>Wing characteristics</u>	<u>Models E and F</u>
Aspect ratio	7.3
Section normal to c/4 line	64A010
Area	233 ft ²
Sweep of c/4 line	40°
Wing incidence	3.4°
Taper ratio	0.49°



(b) Models E and F.

Figure 4.- Concluded.

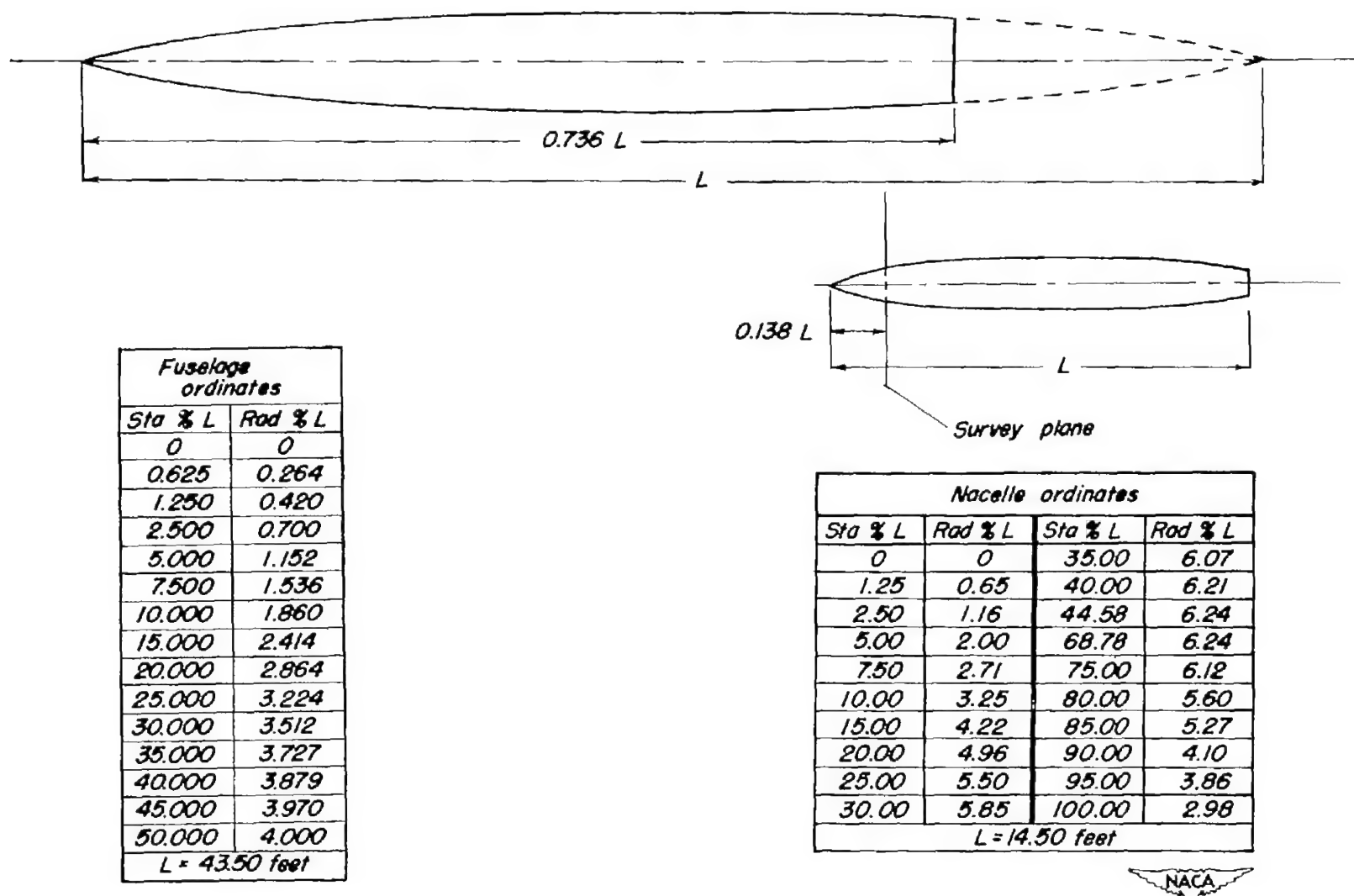
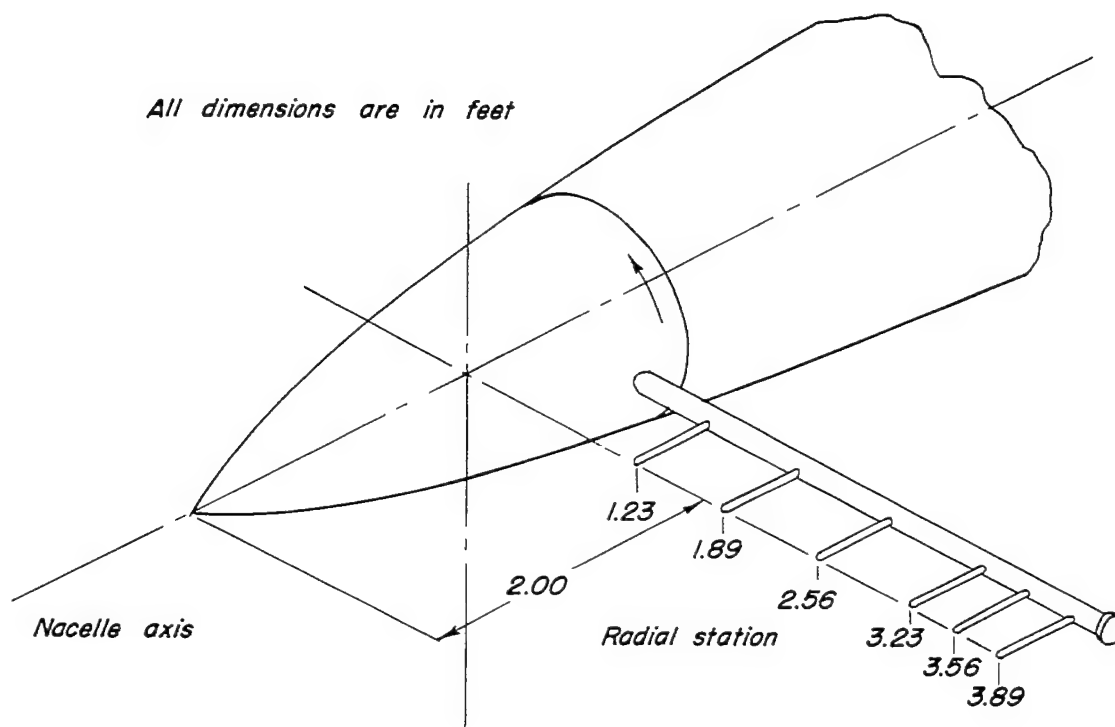
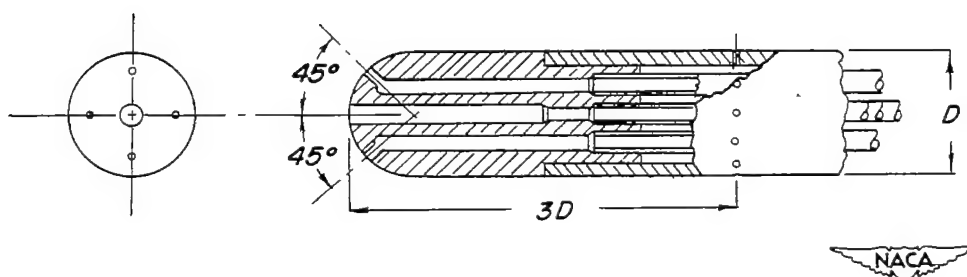


Figure 5.- Geometric characteristics of fuselage and nacelle.

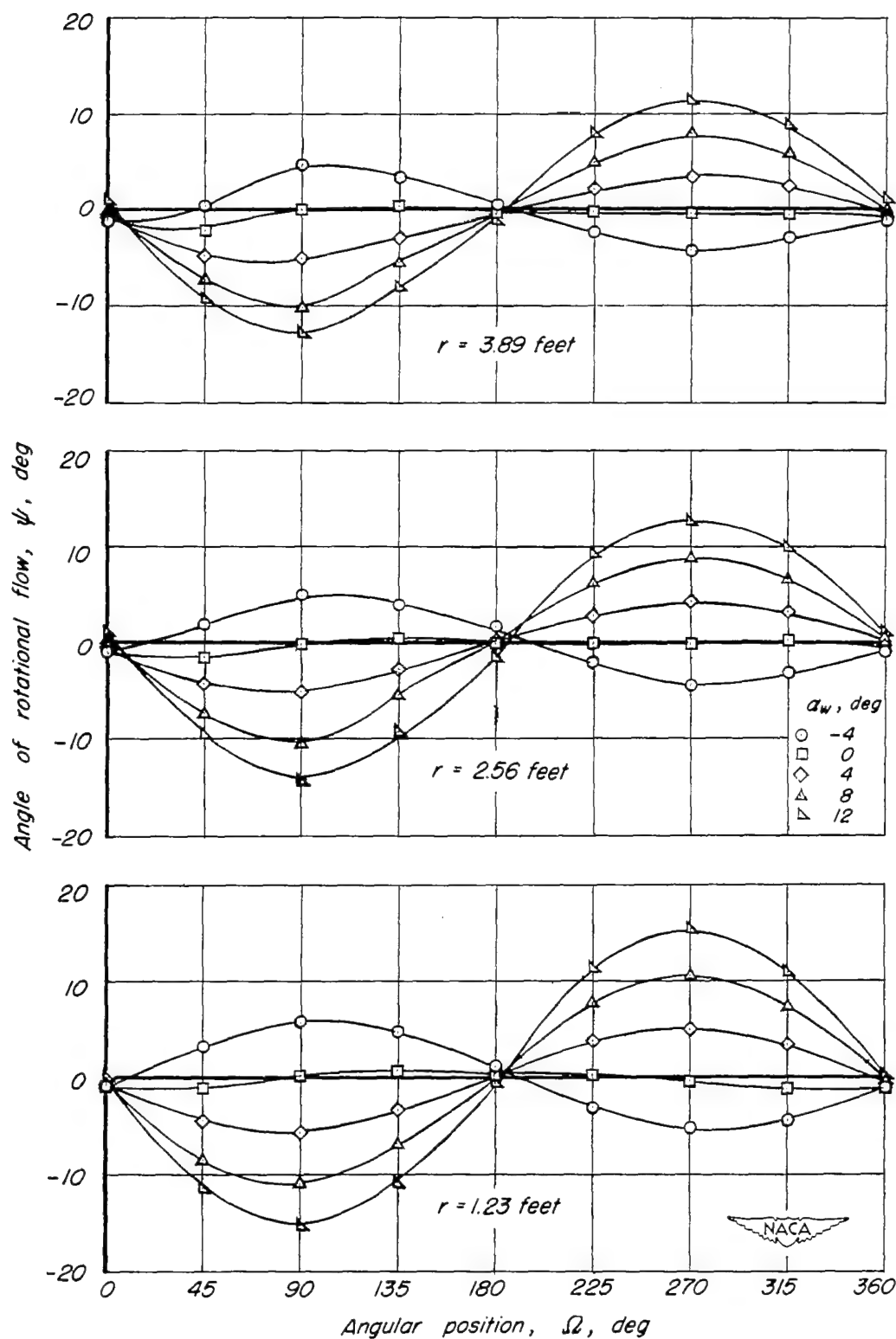


(a) Radial distribution of tubes.



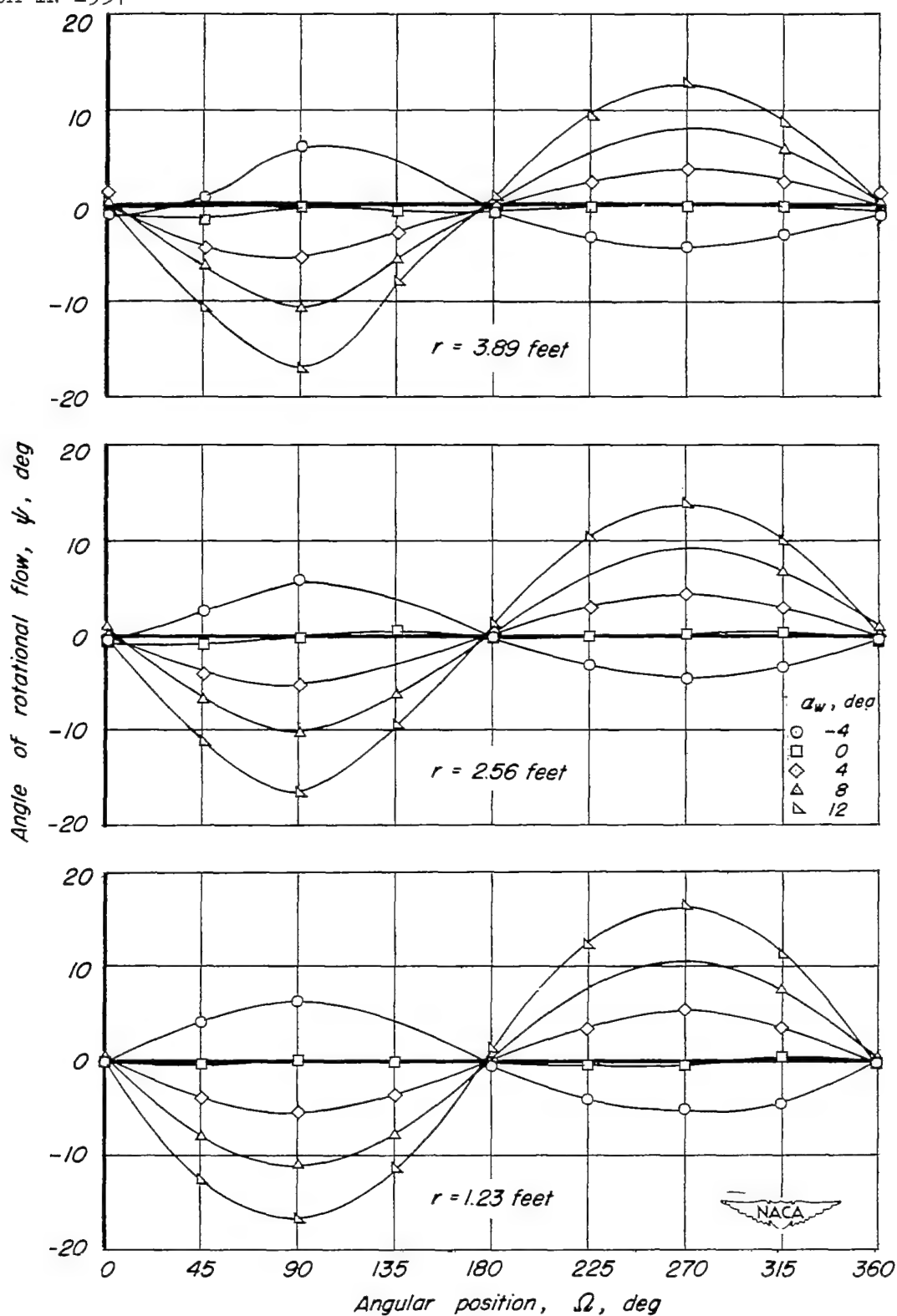
(b) Directional pitot-static-tube head.

Figure 6.— Details of the survey rake.



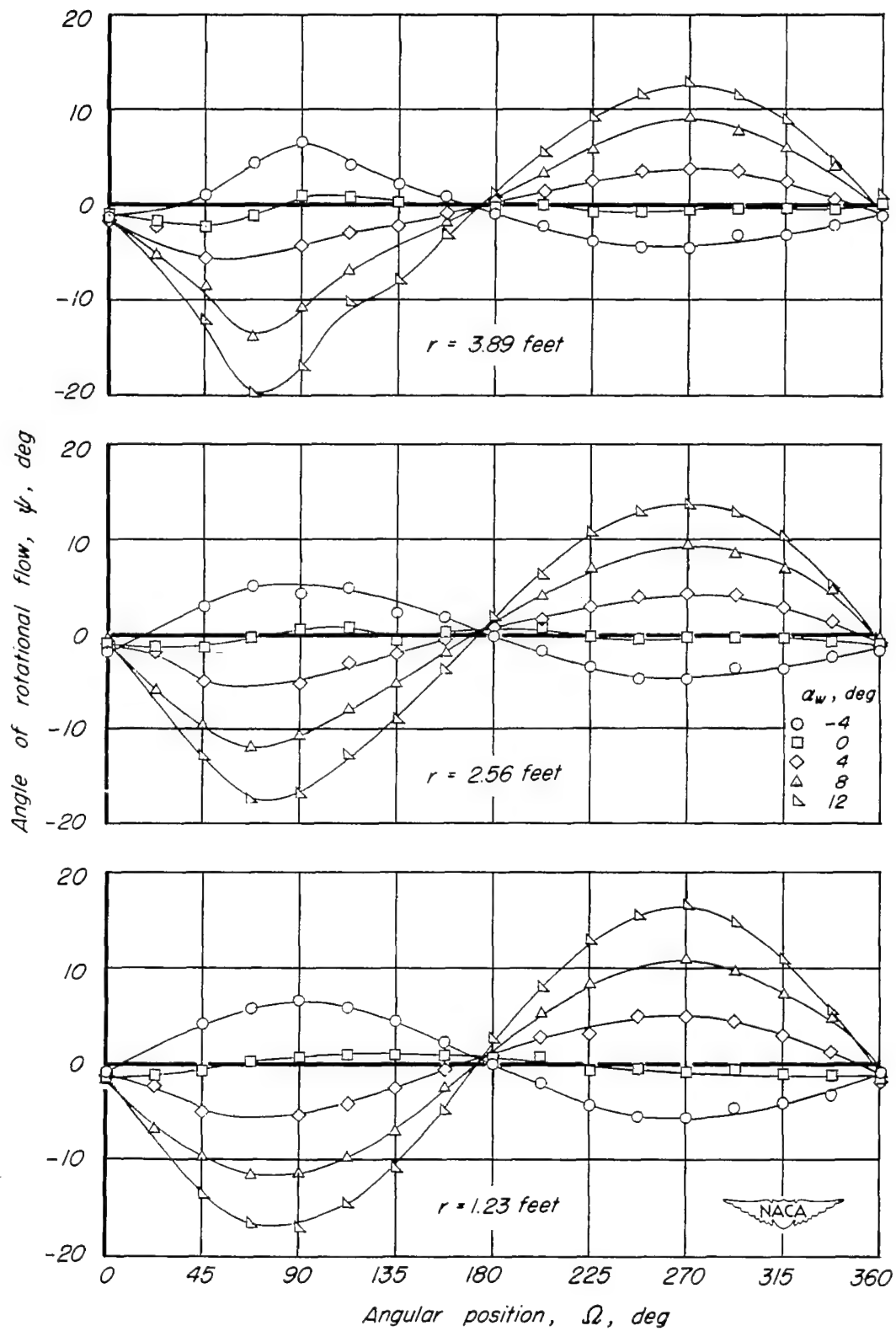
(a) Model A, inboard survey disk.

Figure 7.— Variation of the angle of rotational flow ψ with angular position for several angles of attack.

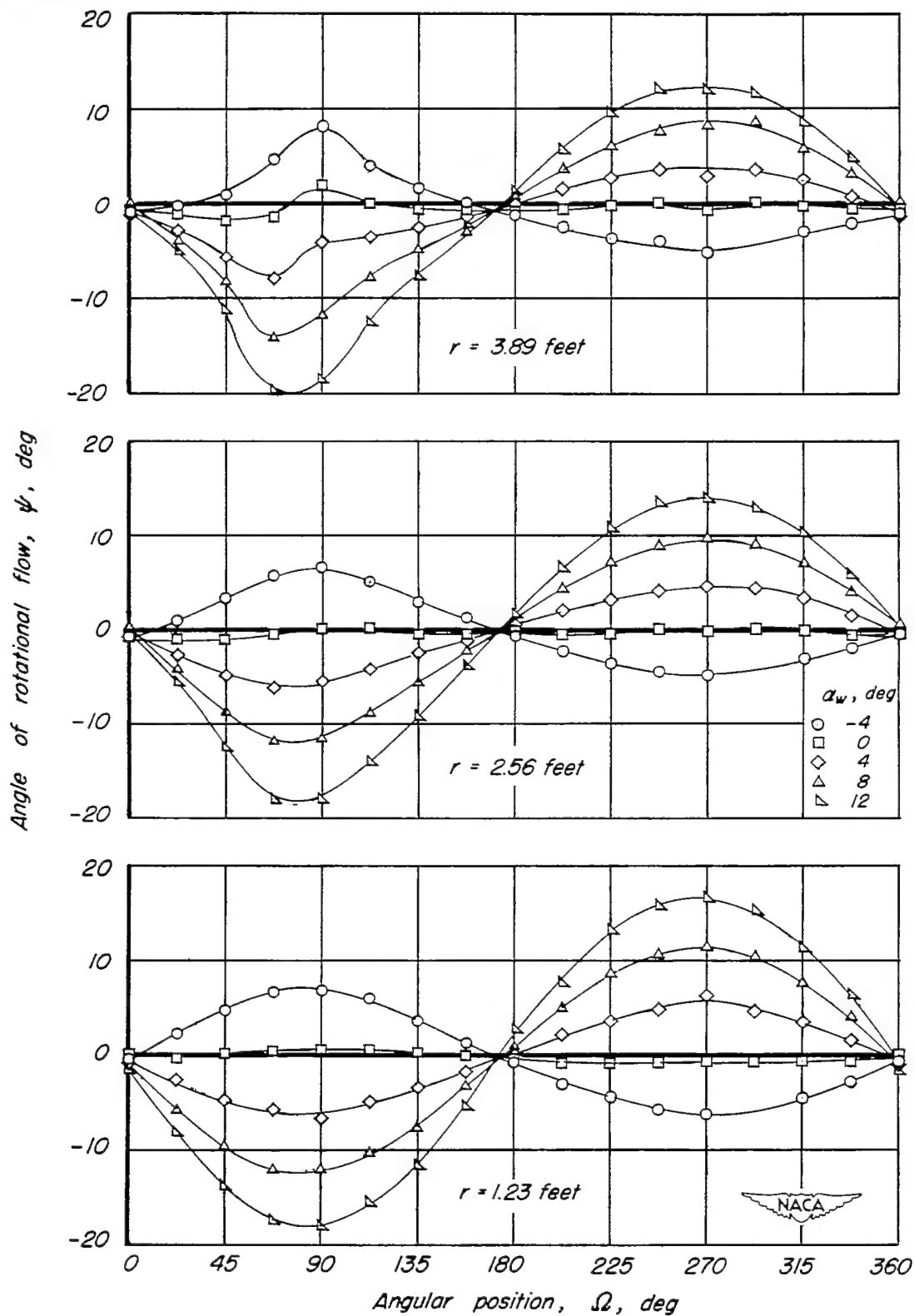


(b) Model A, outboard survey disk.

Figure 7.— Continued.

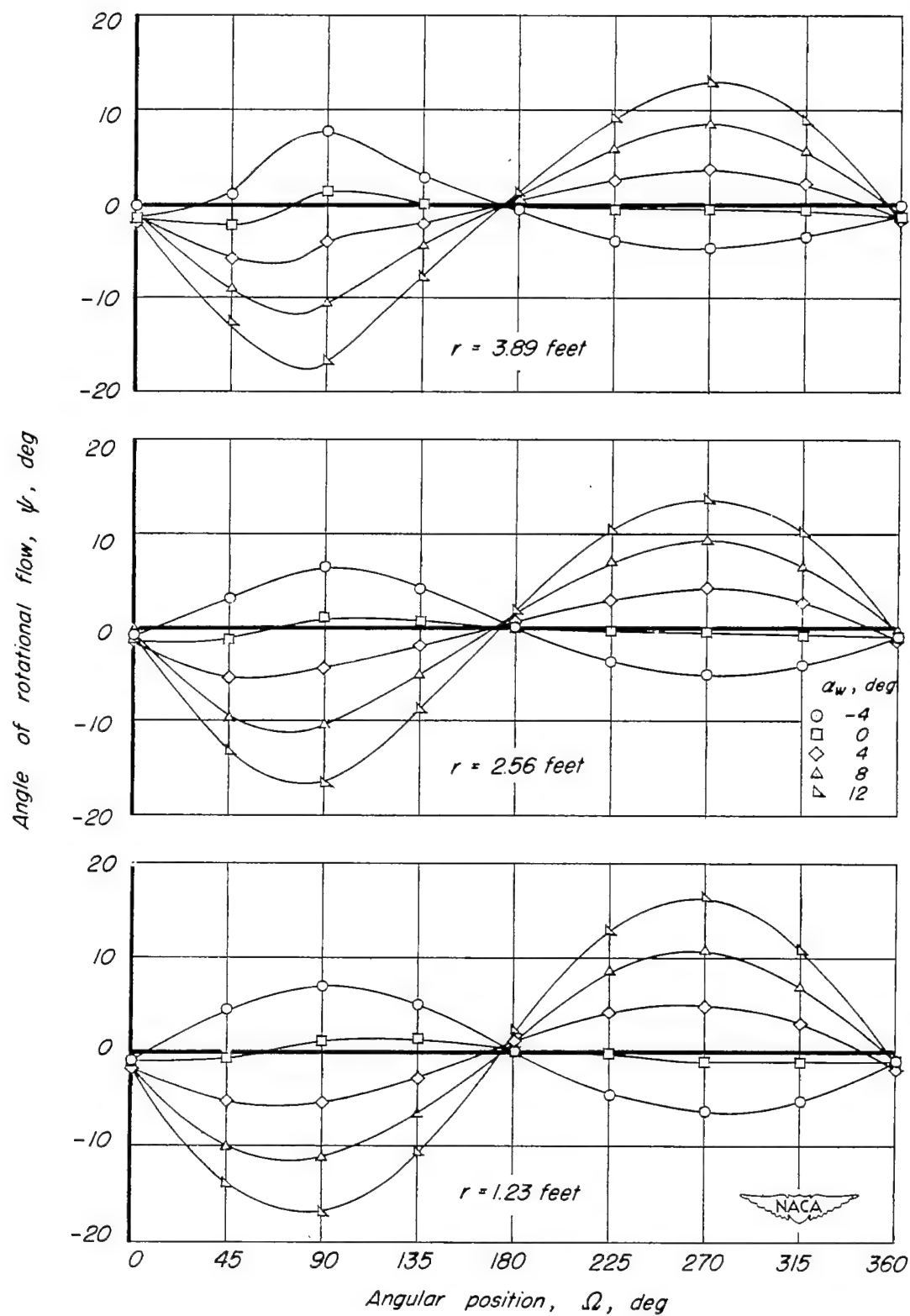


(c) Model B, inboard survey disk.
Figure 7. — Continued.



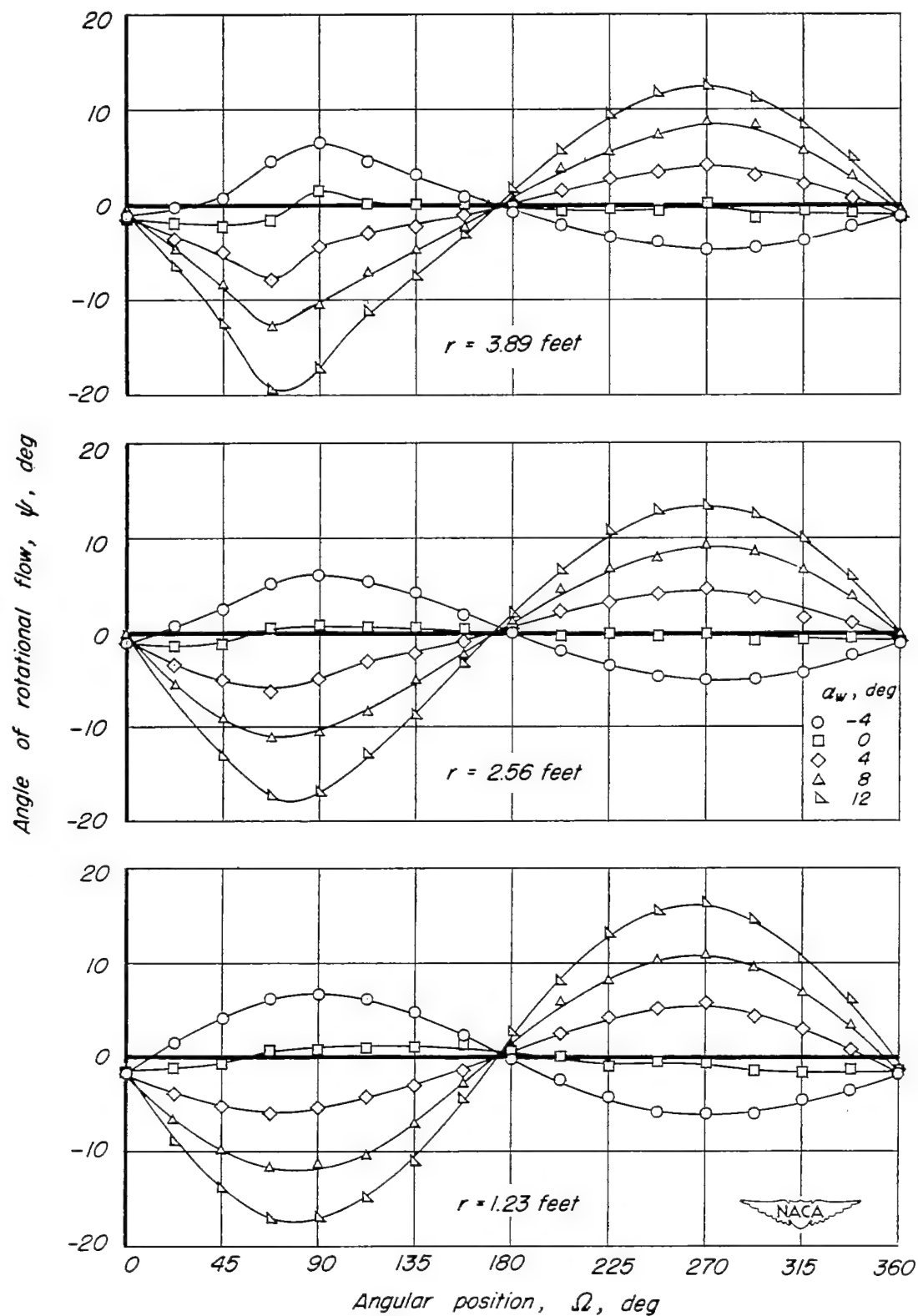
(d) Model B, outboard survey disk.

Figure 7.— Continued.



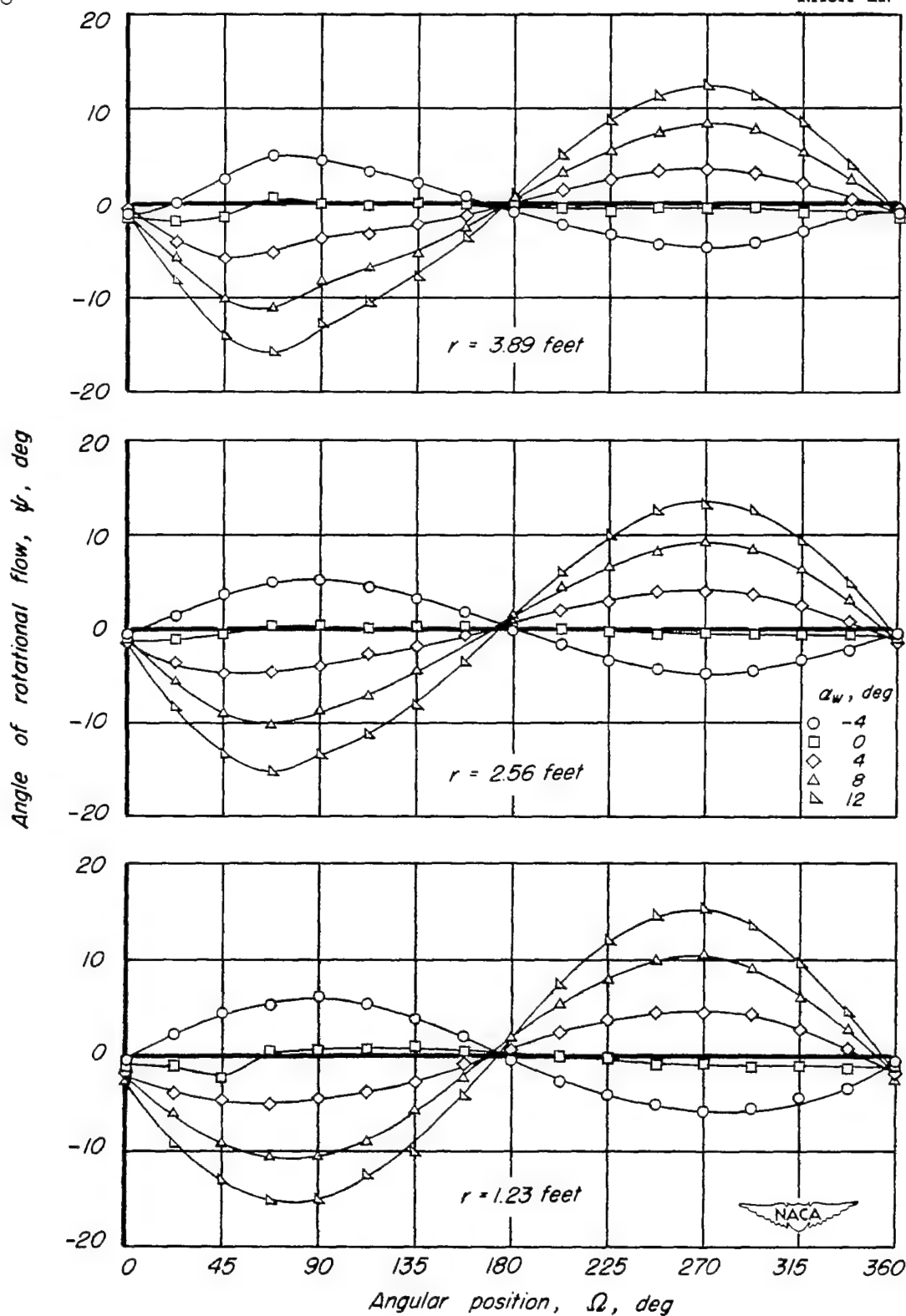
(e) Model C, inboard survey disk.

Figure 7. — Continued.

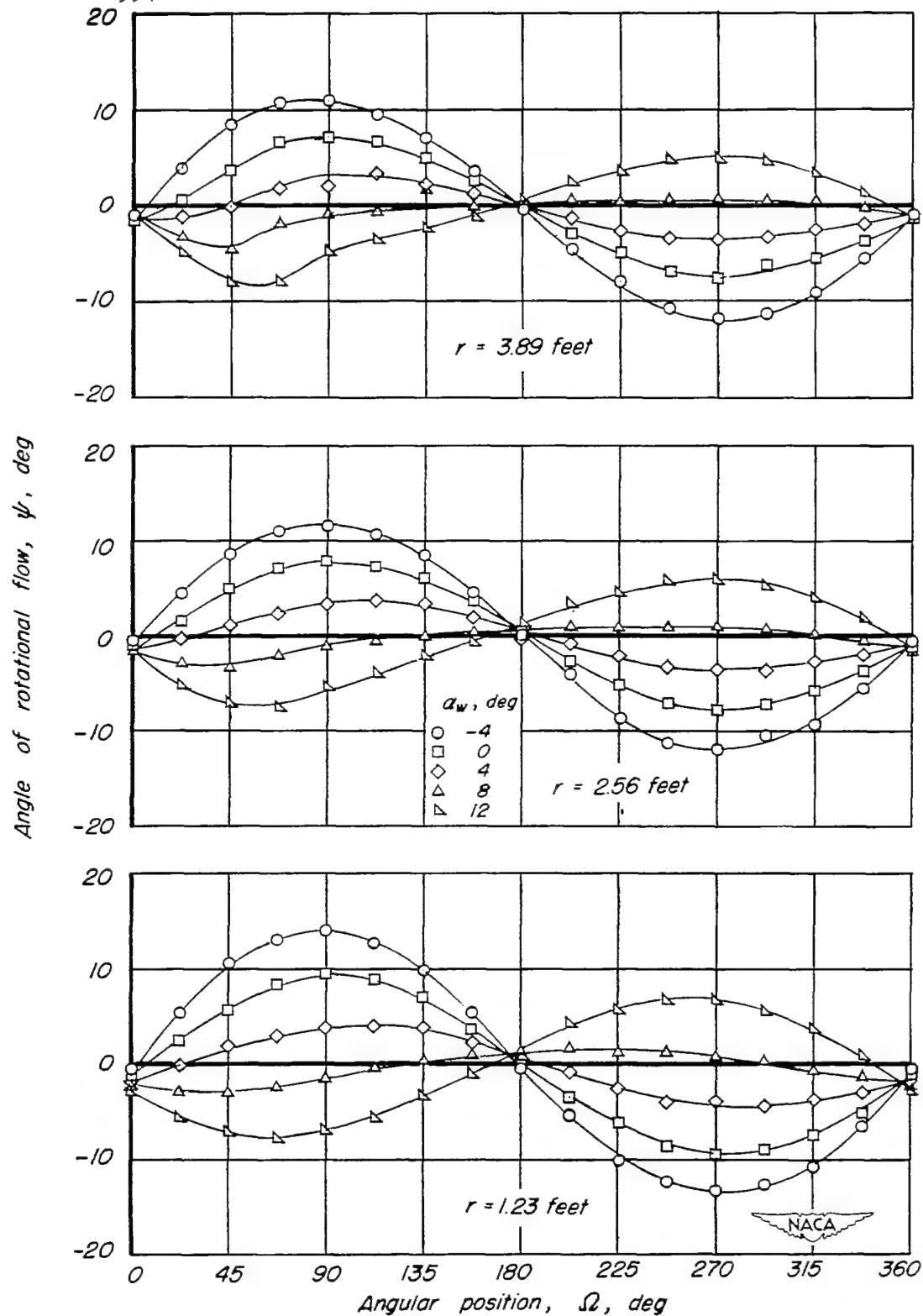


(f) Model D.

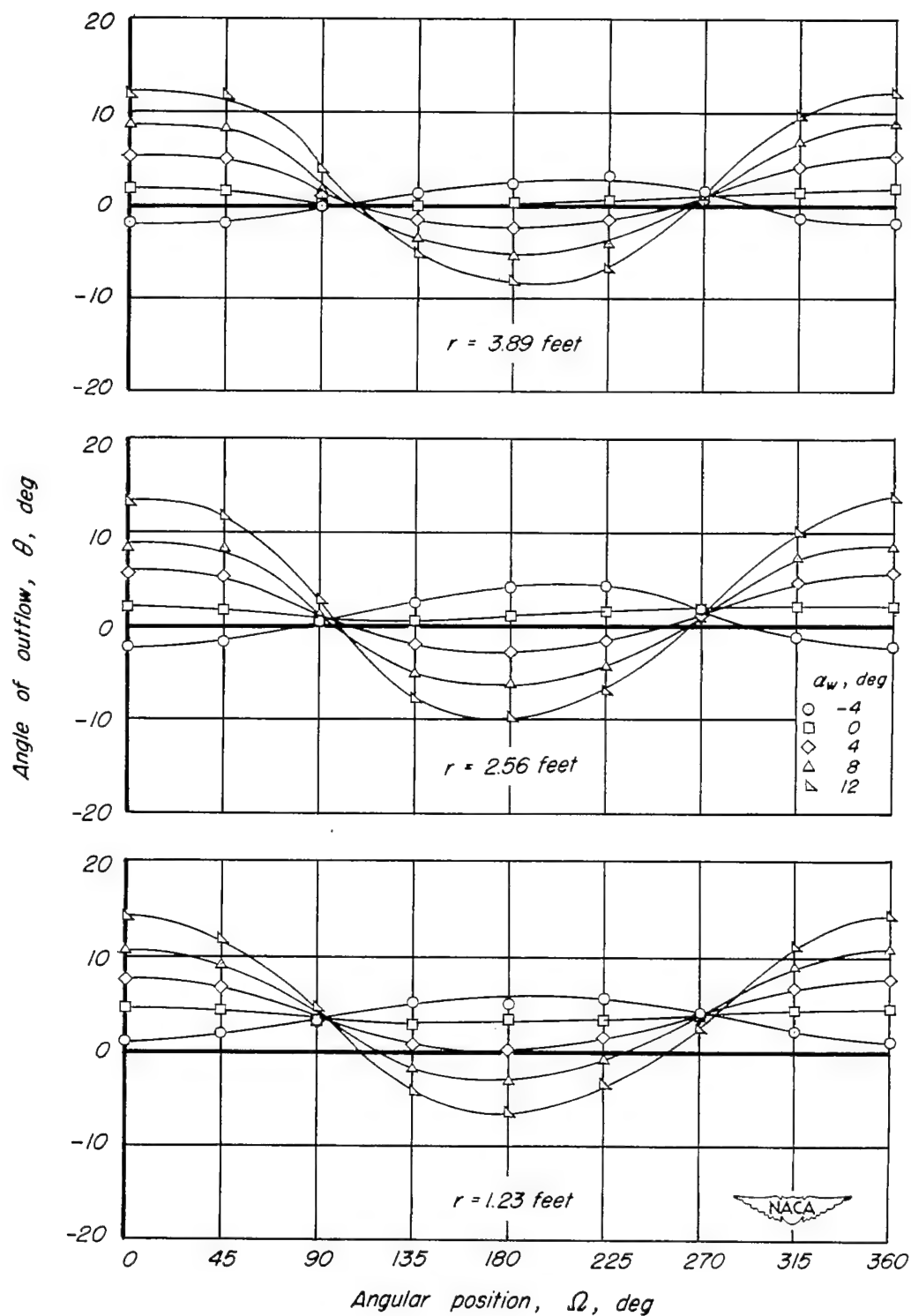
Figure 7. — Continued.



(g) Model E.
Figure 7. — Continued.

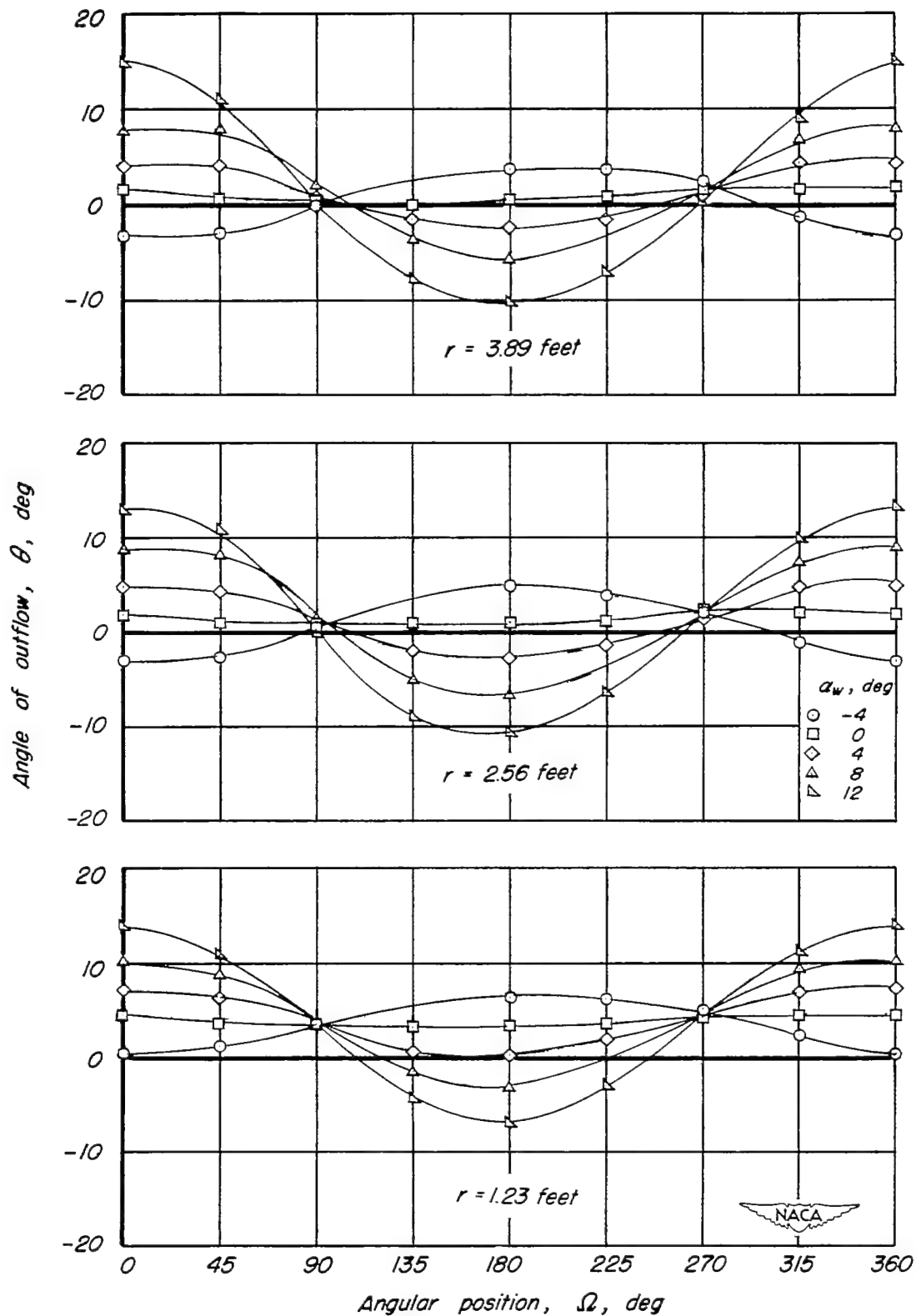


(h) Model F.
Figure 7.— Concluded.

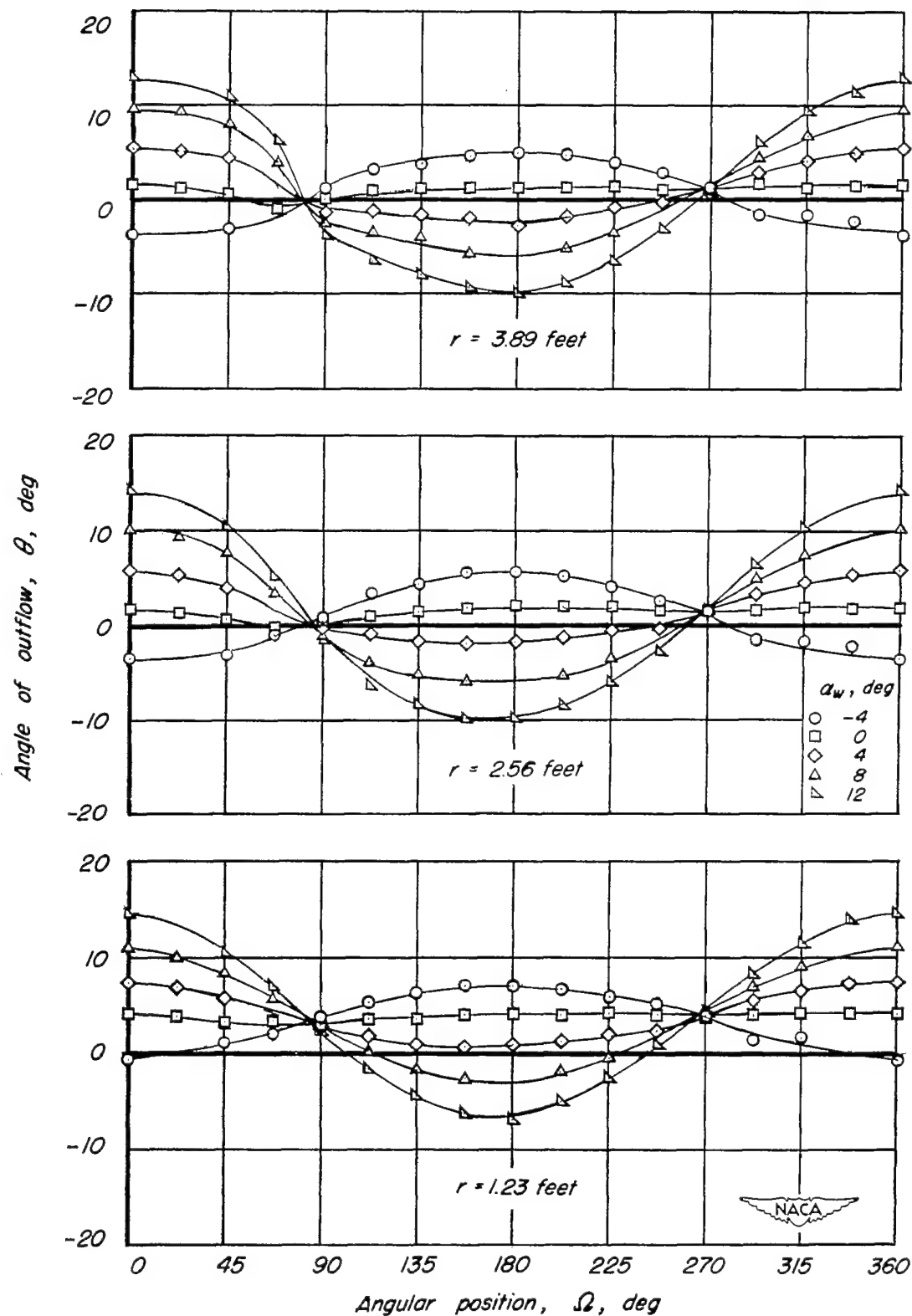


(a) Model A, inboard survey disk.

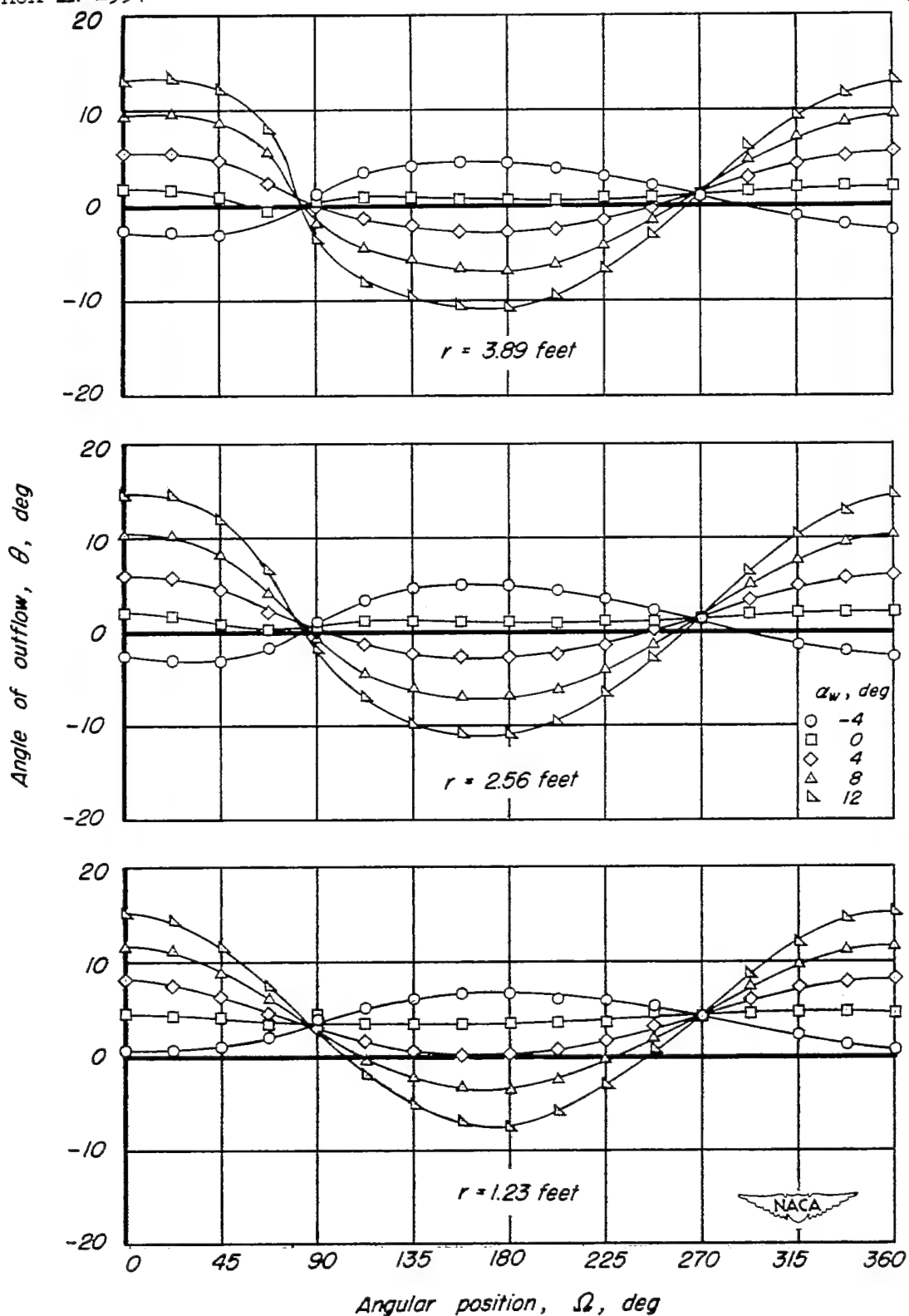
Figure 8.— Variation of the angle of outflow θ with angular position for several angles of attack.



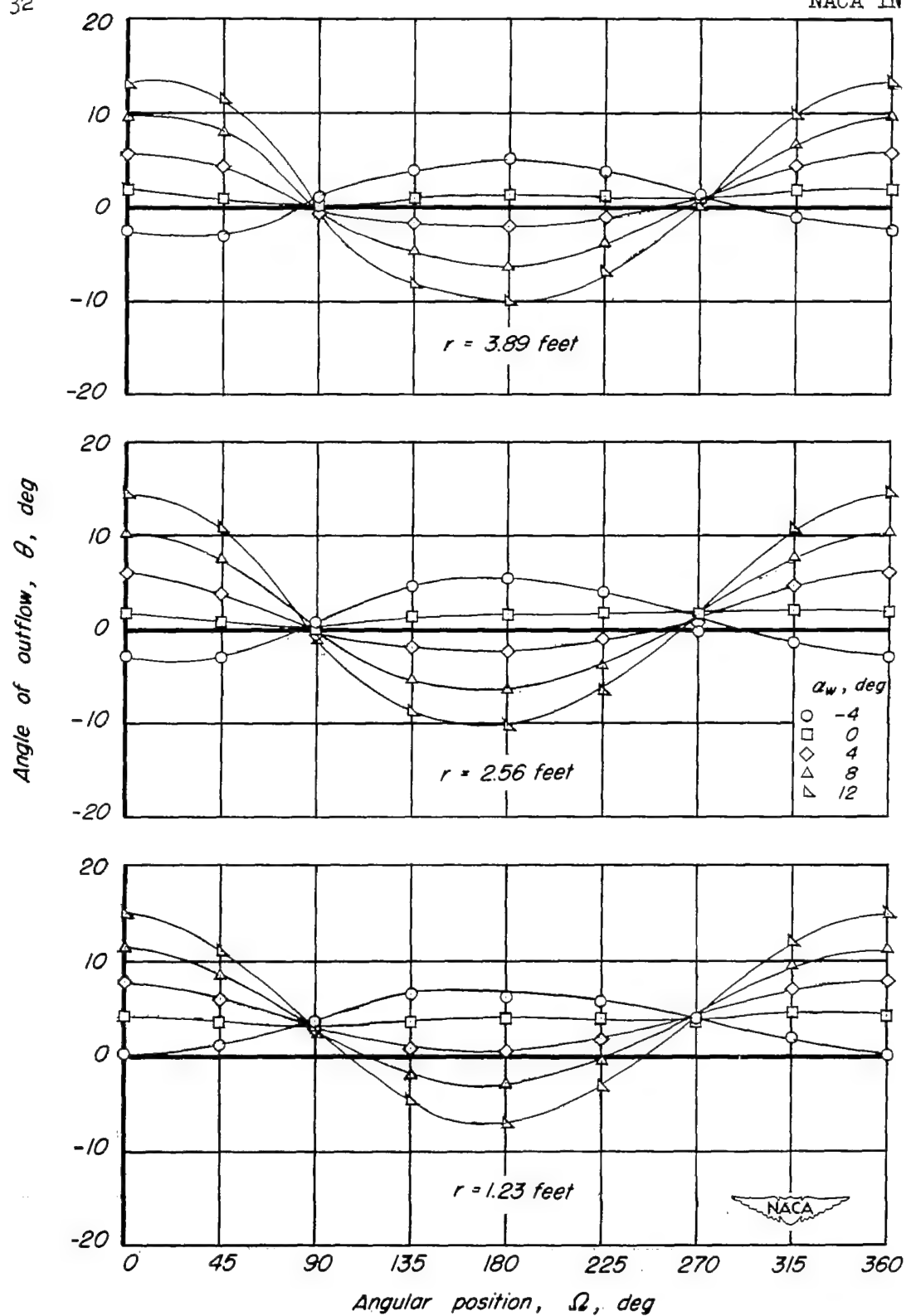
(b) Model A, outboard survey disk.
Figure 8.— Continued.



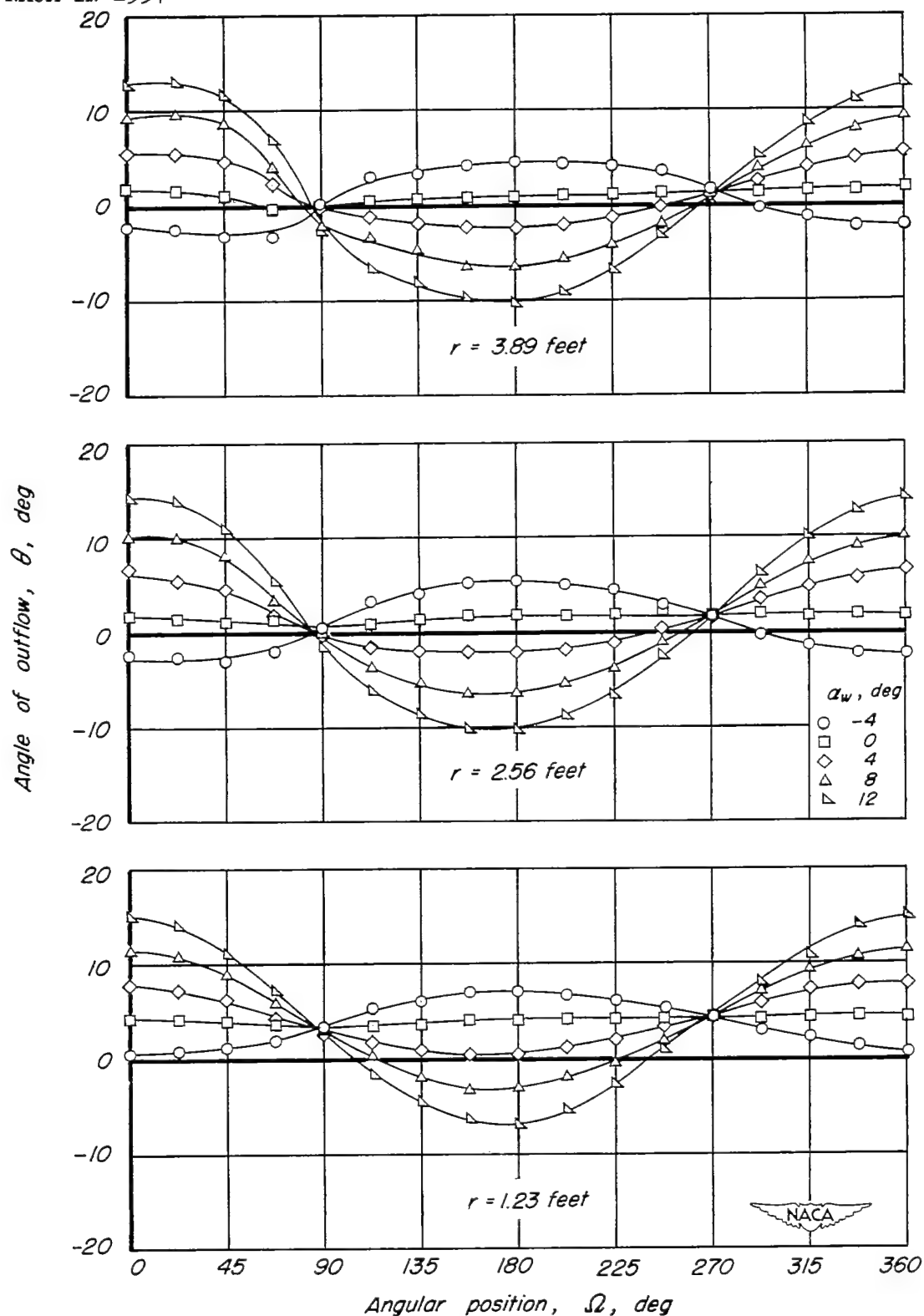
(c) Model B, inboard survey disk.
Figure 8.— Continued.



(d) Model B, outboard survey disk.
Figure 8.— Continued.

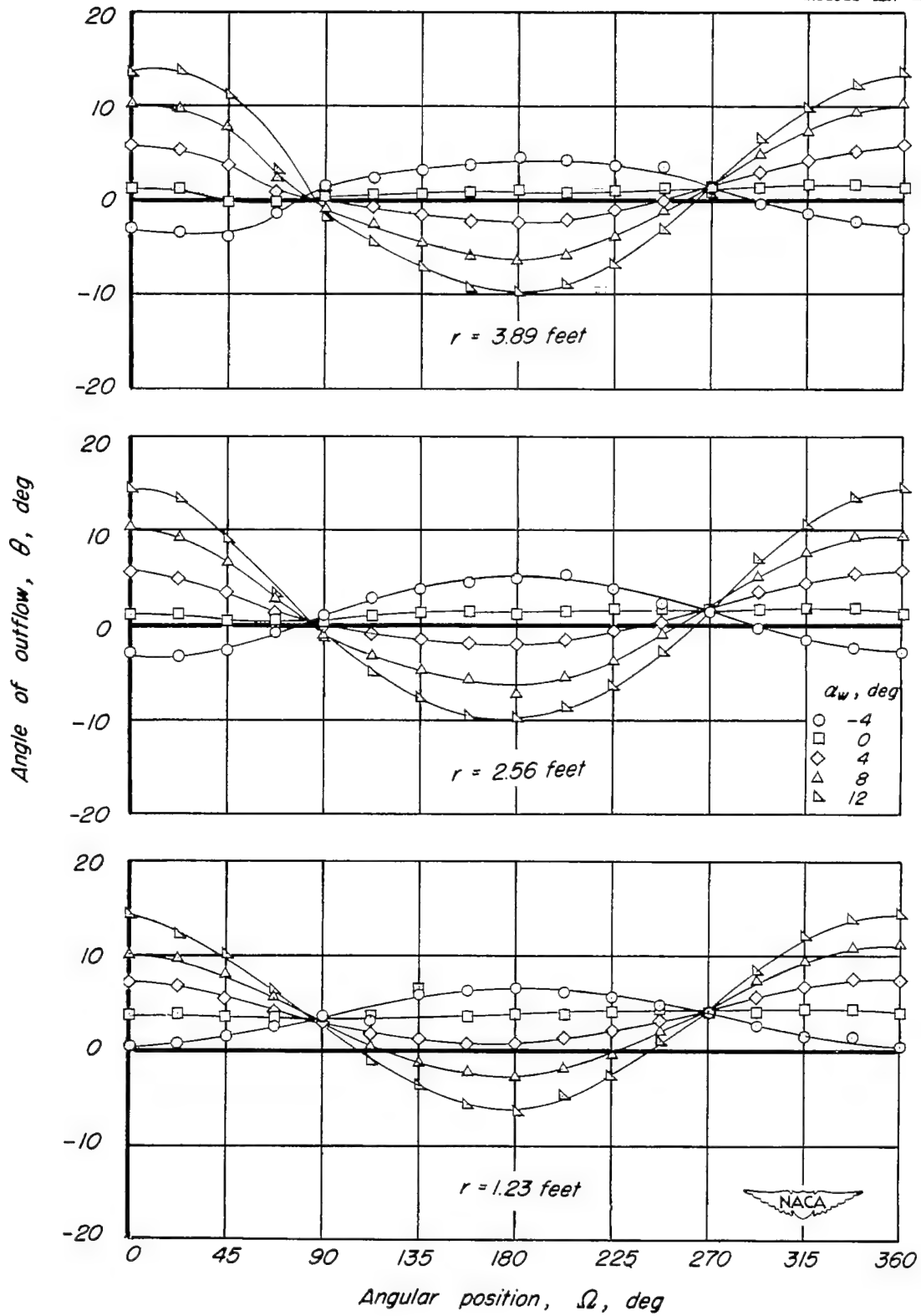


(a) Model C, inboard survey disk.
Figure 8. — Continued.

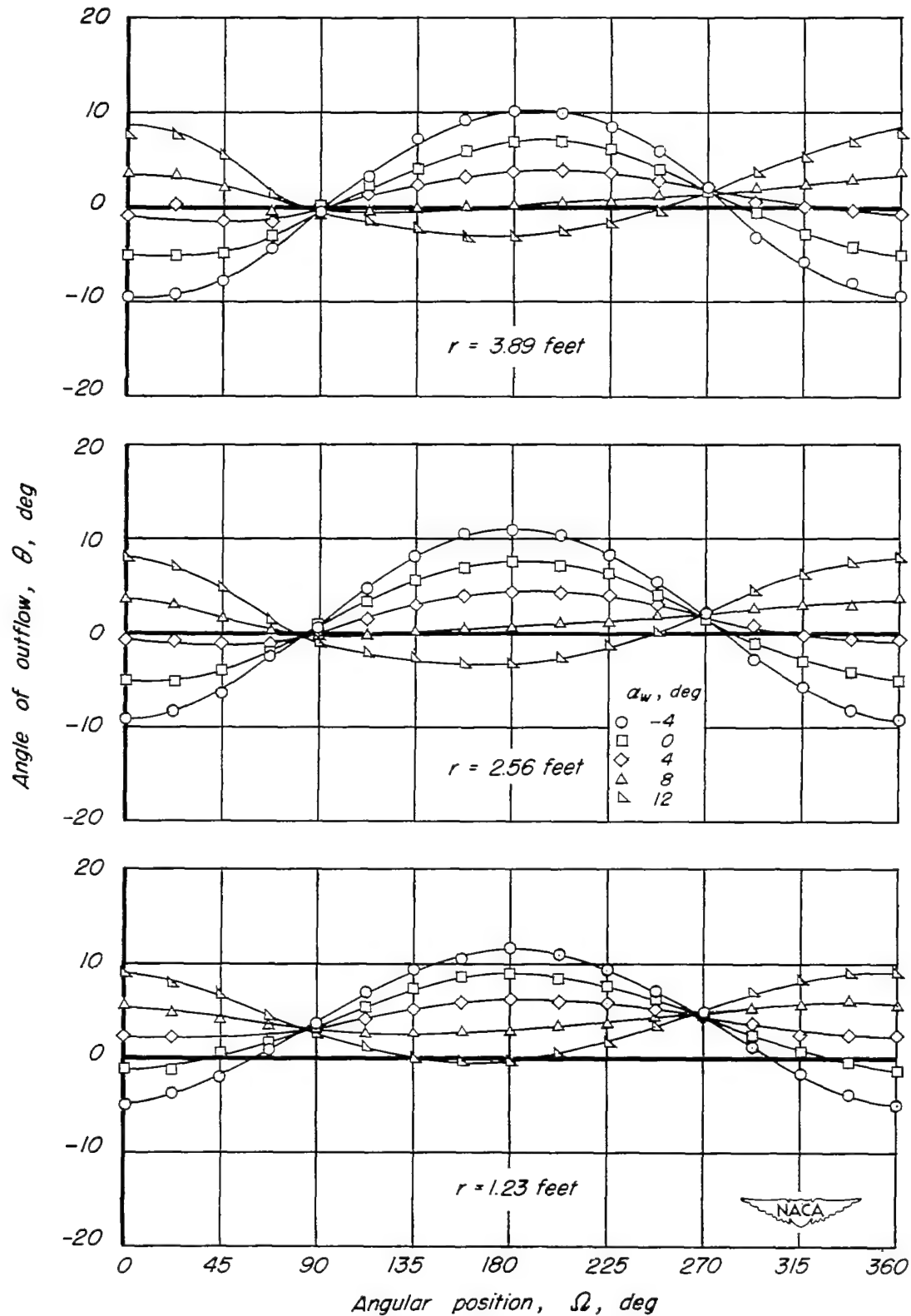


(f) Model D.

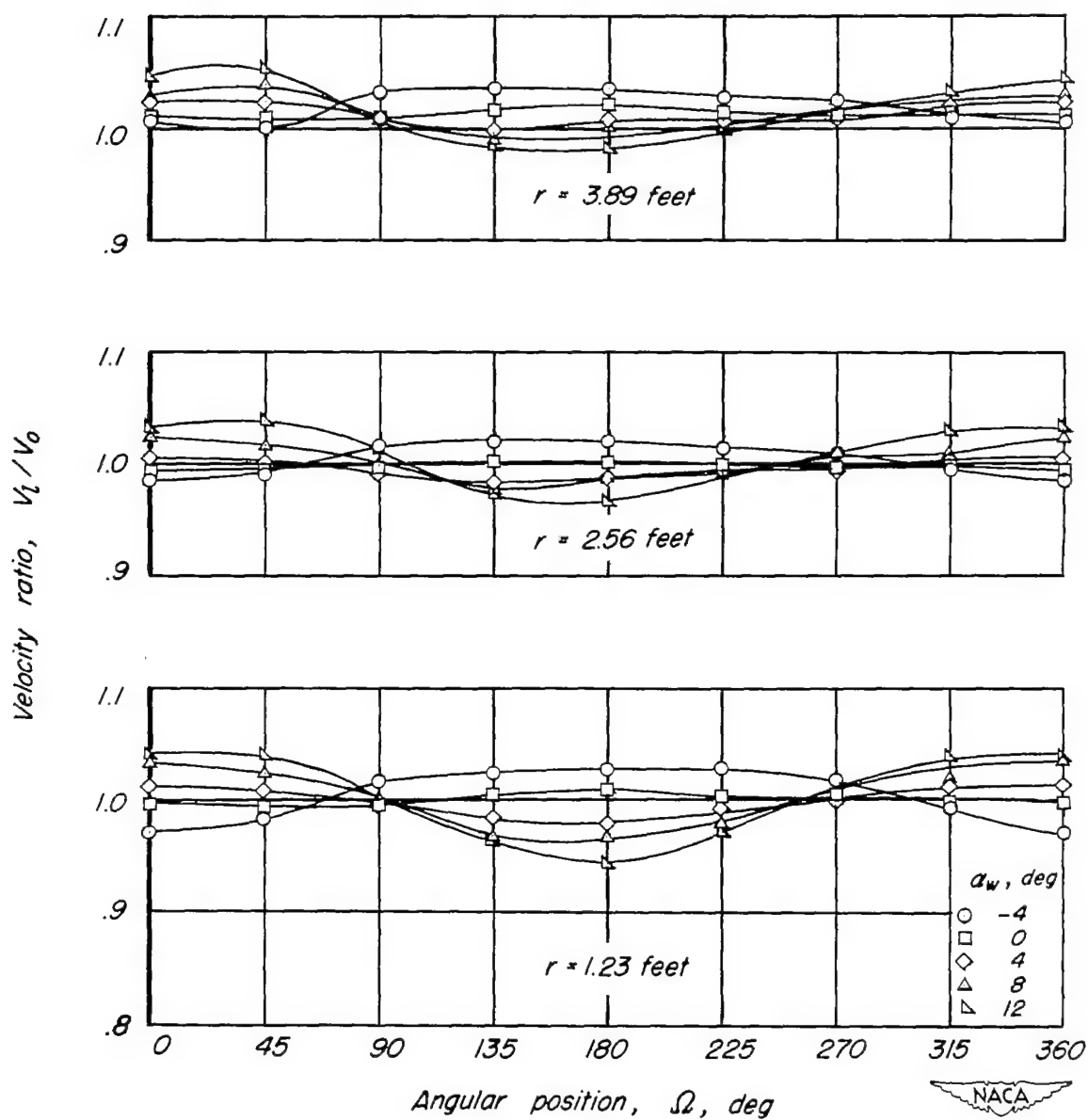
Figure 8. — Continued.



(g) Model E.
Figure 8. — Continued.

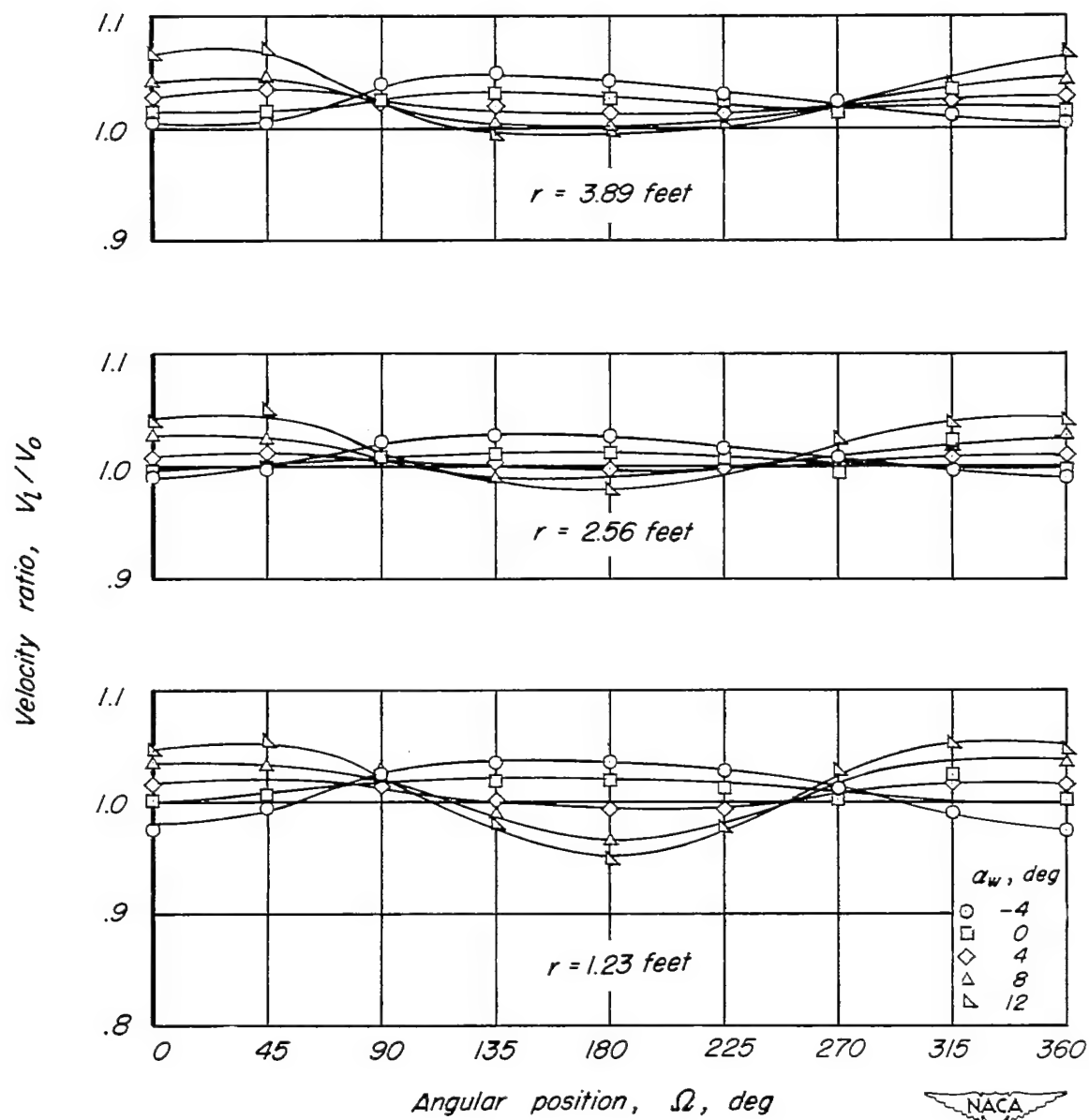


(h) Model F.
Figure 8.— Concluded.



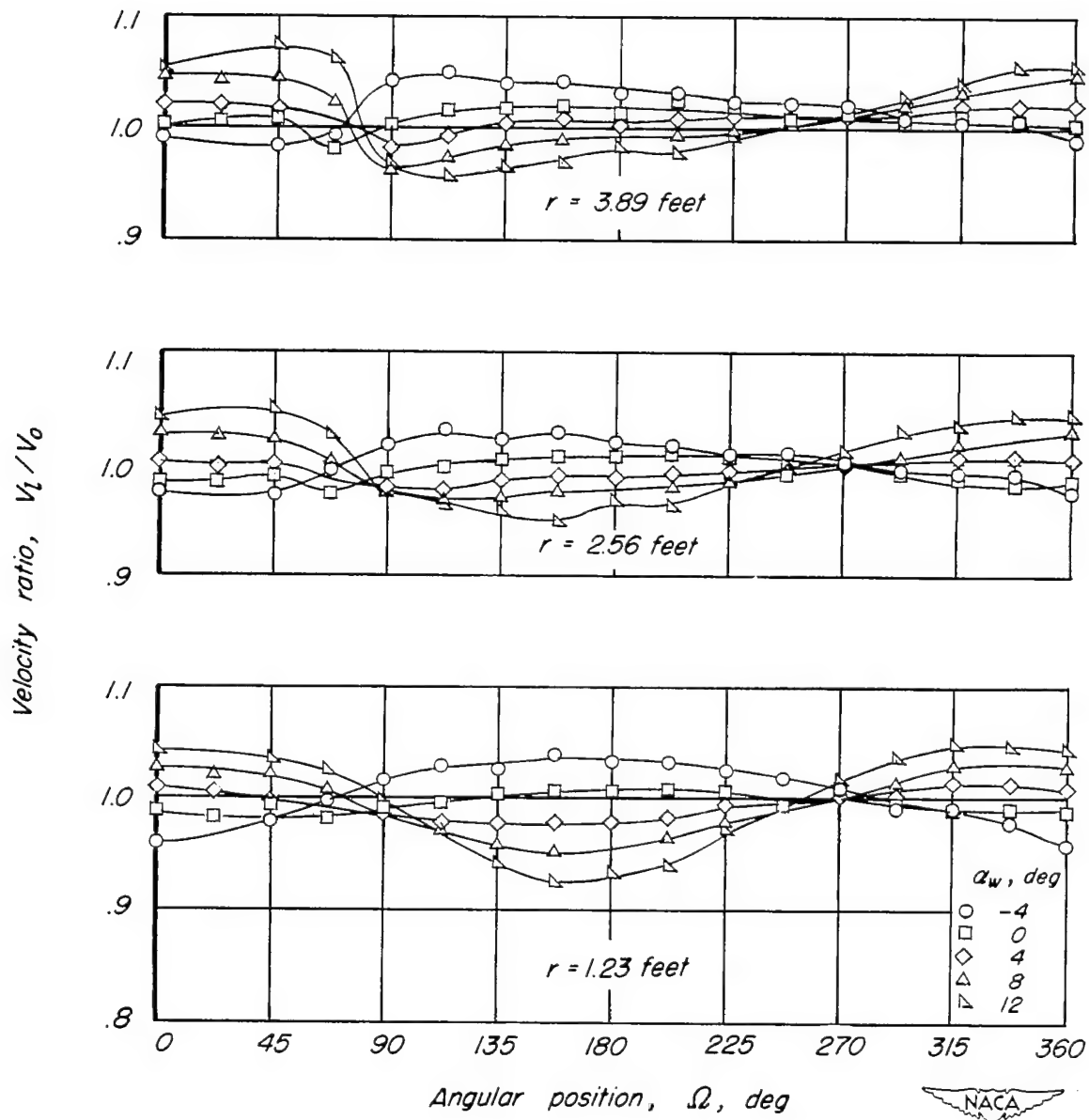
(a) Model A, inboard survey disk.

Figure 9.— Variation of the velocity V_t/V_0 with angular position for several angles of attack.



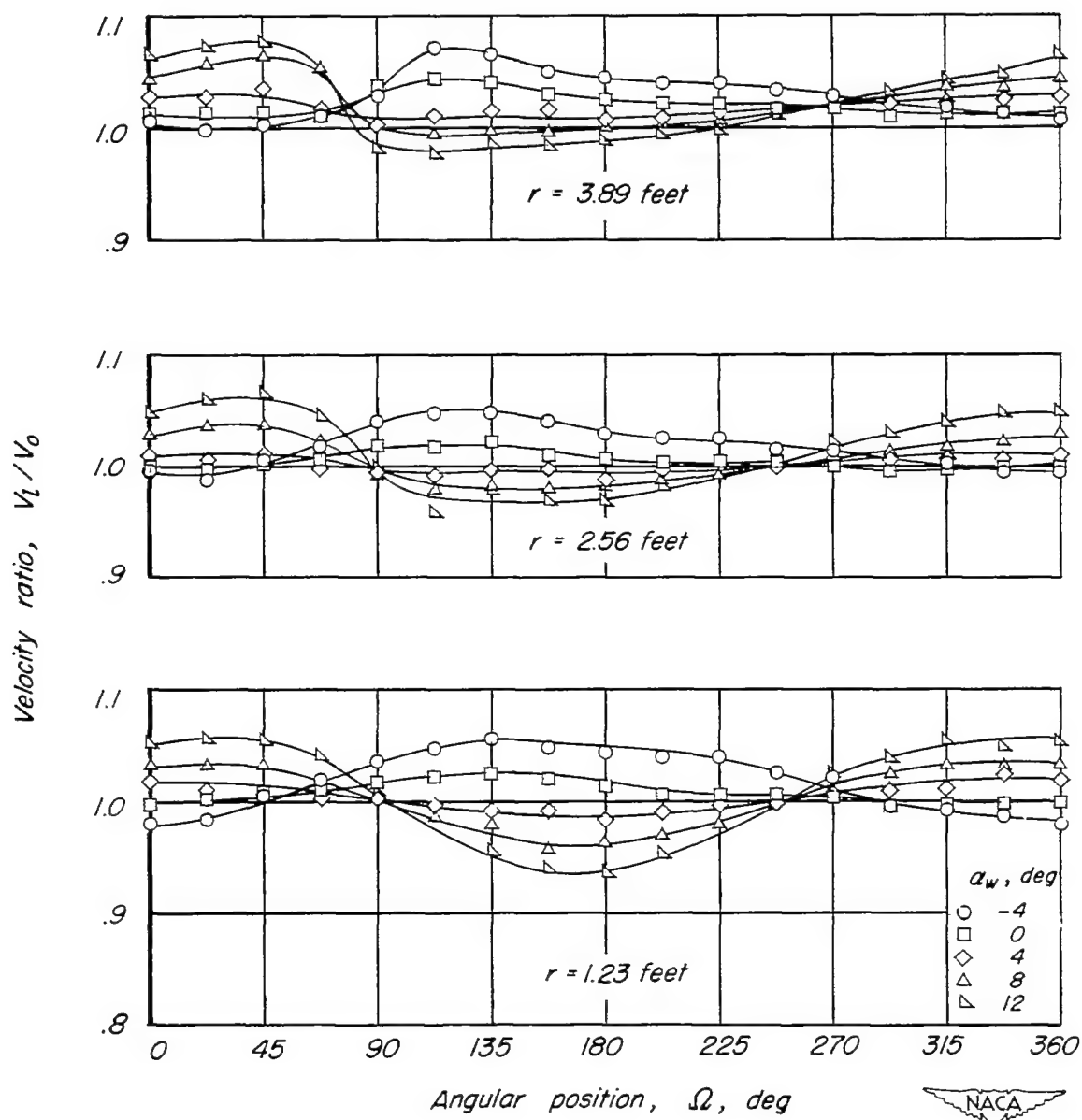
(b) Model A, outboard survey disk.

Figure 9. — Continued.



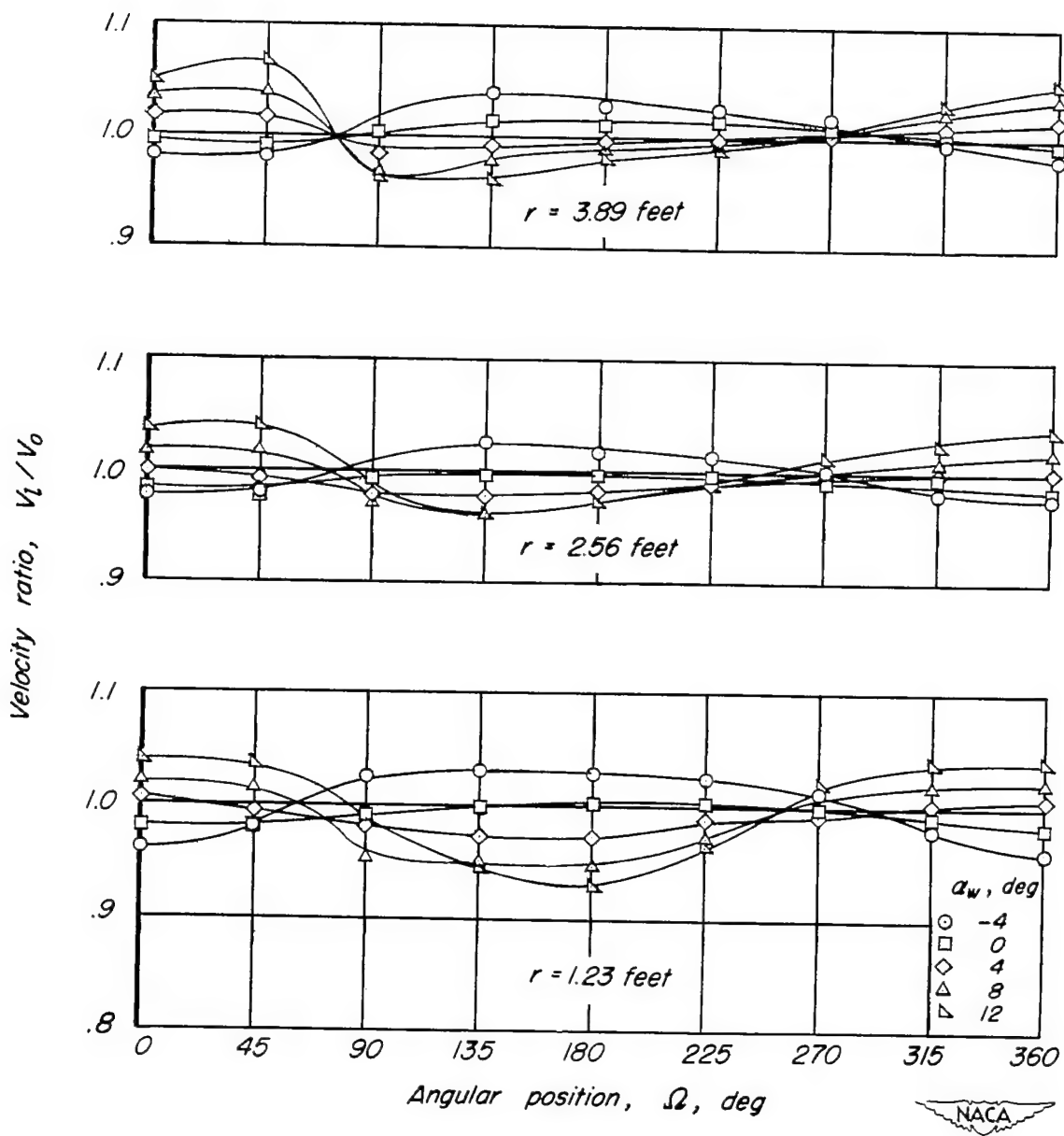
(c) Model B, inboard survey disk.

Figure 9. — Continued.



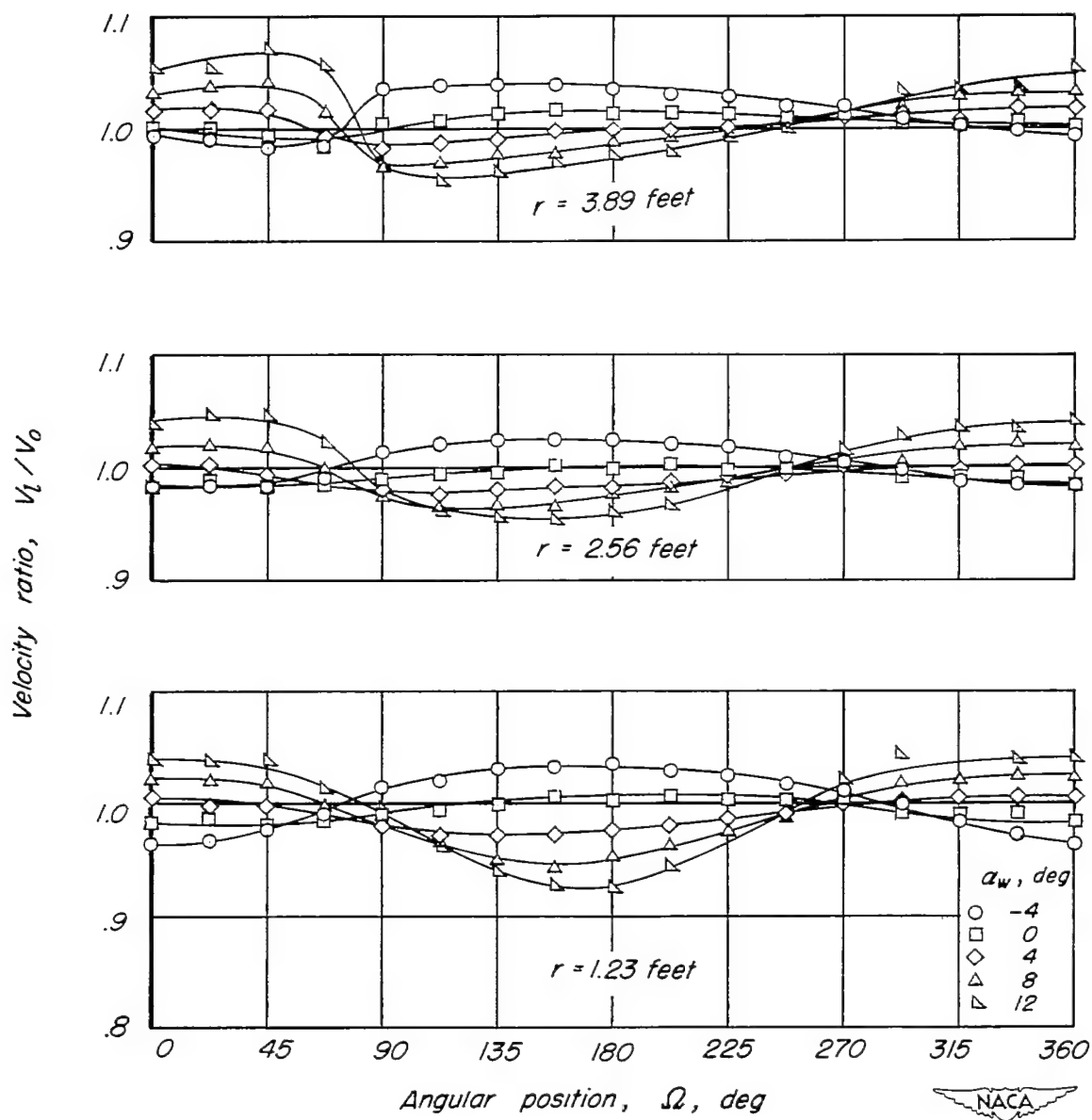
(d) Model B, outboard survey disk.

Figure 9. — Continued.



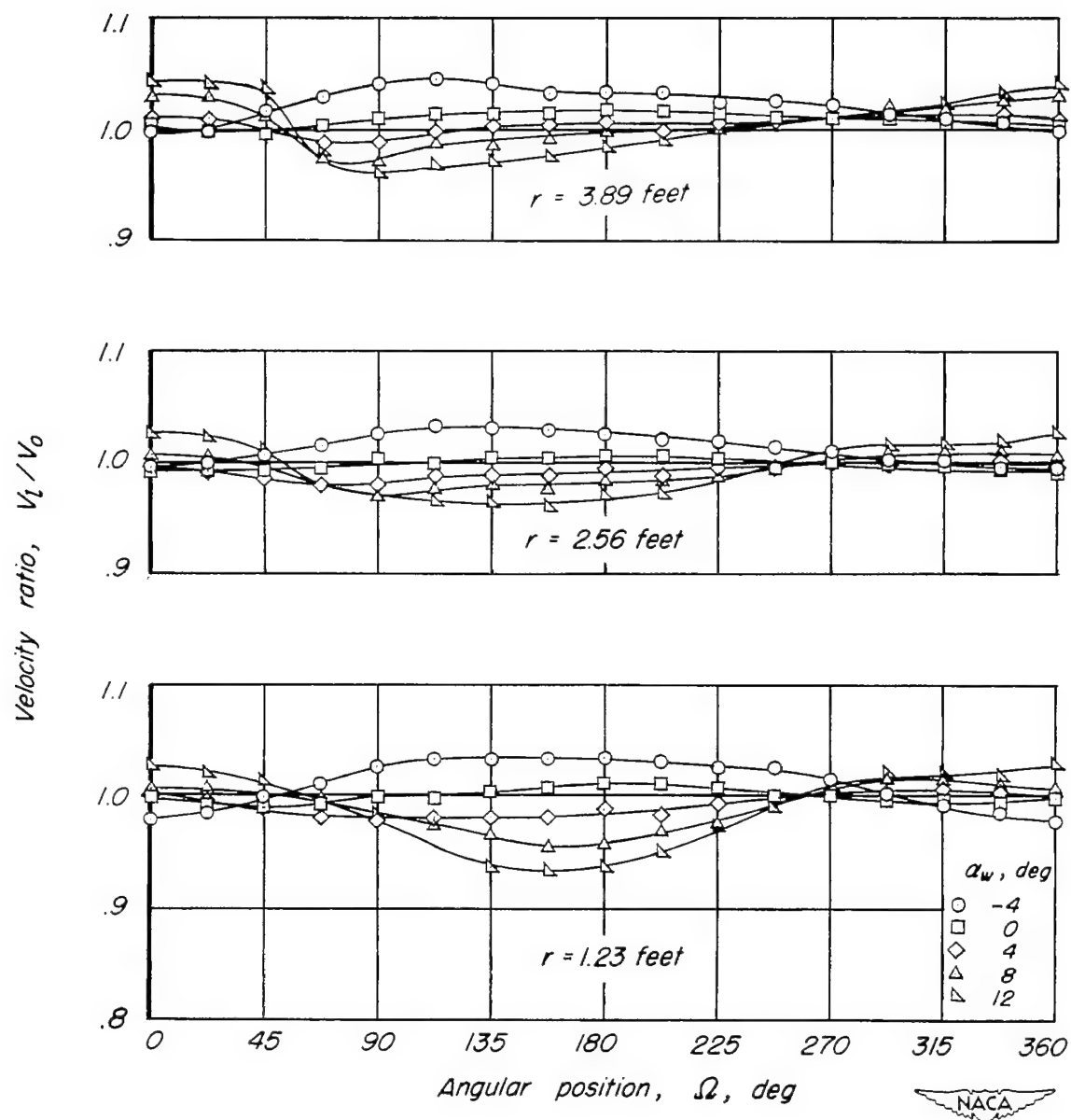
(e) Model C, inboard survey disk.

Figure 9.—Continued.

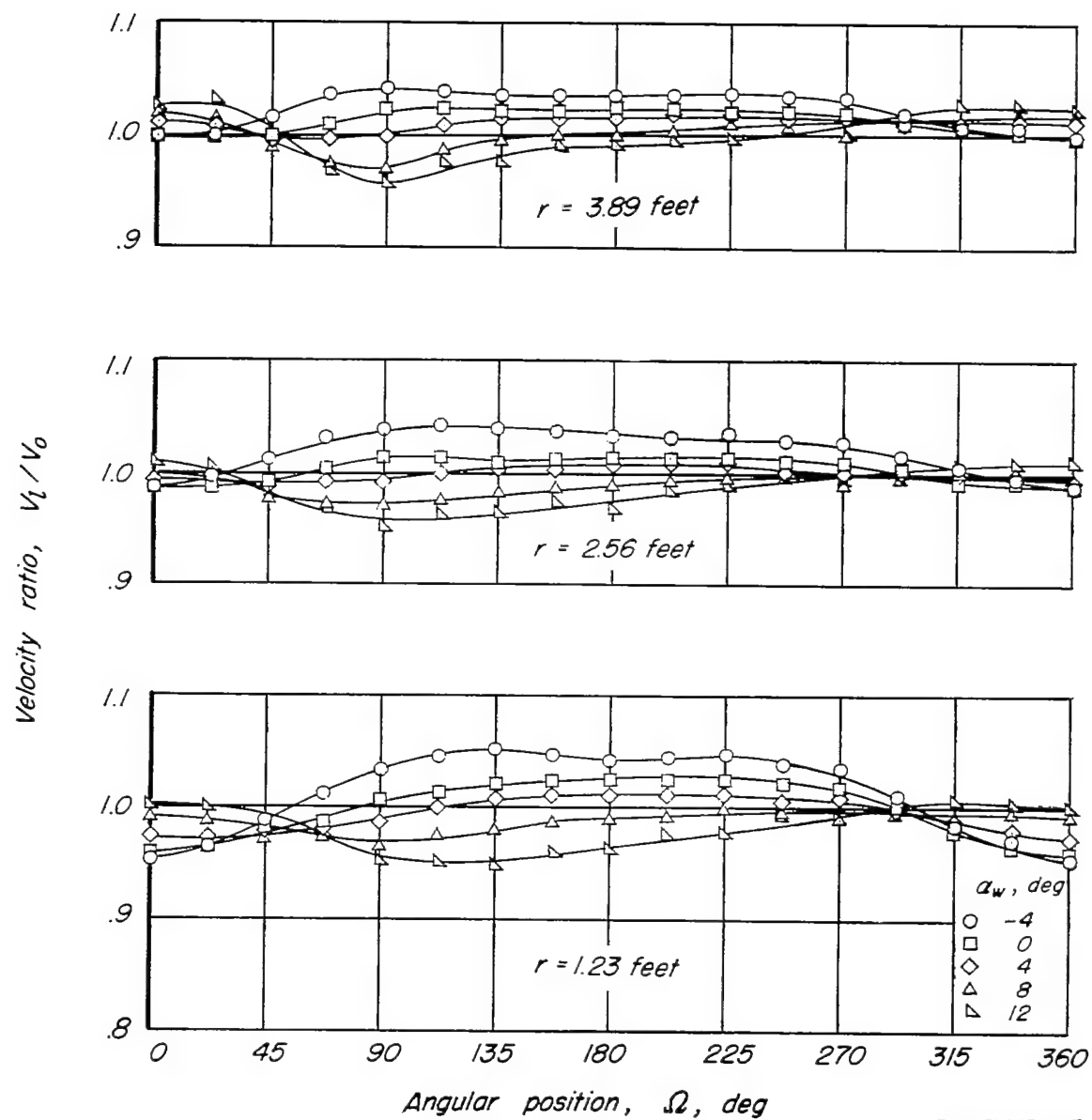


(f) Model D.

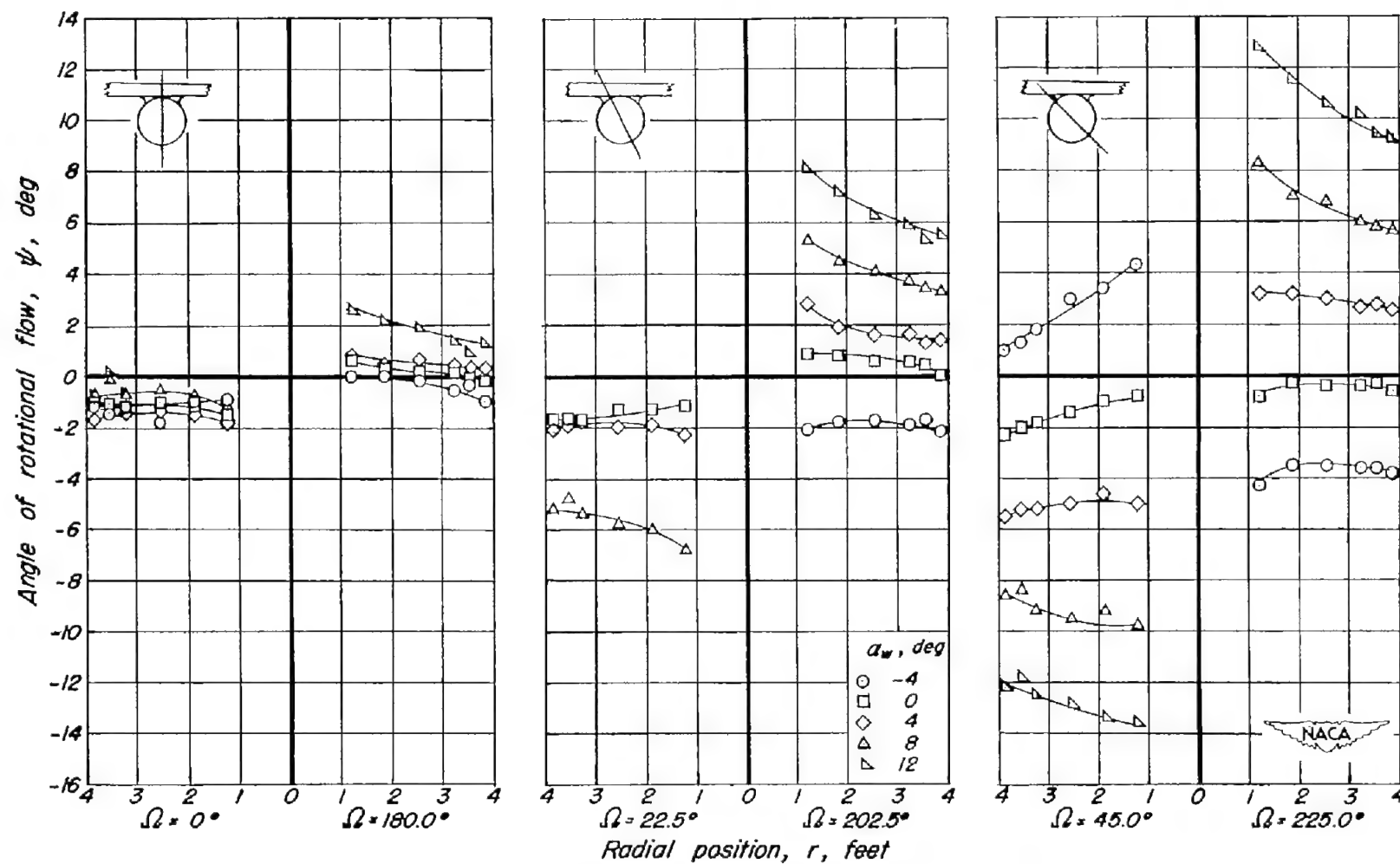
Figure 9.—Continued.



(g) Model E.
Figure 9.— Continued.

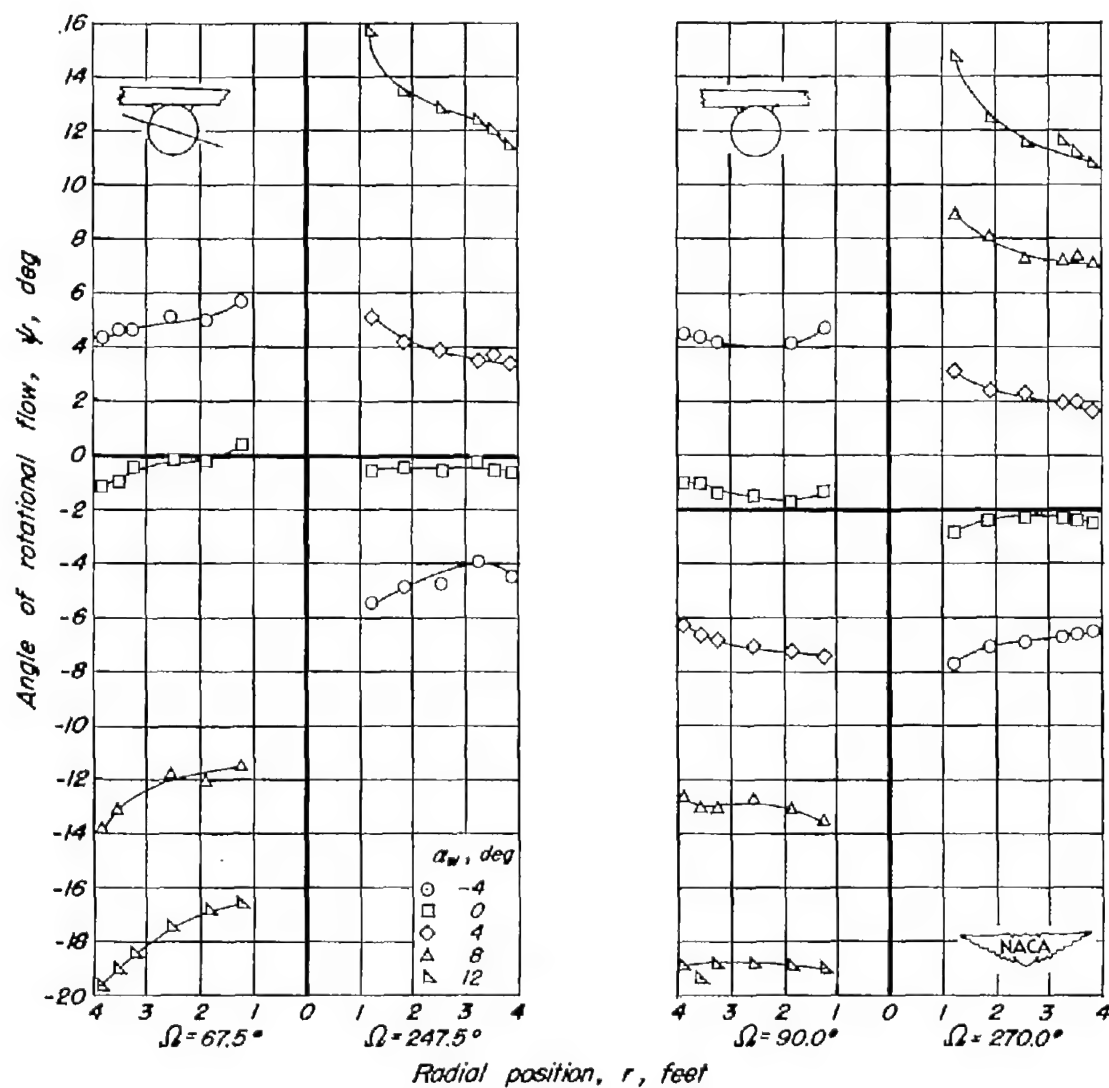


(h) Model F.
Figure 9.—Concluded.

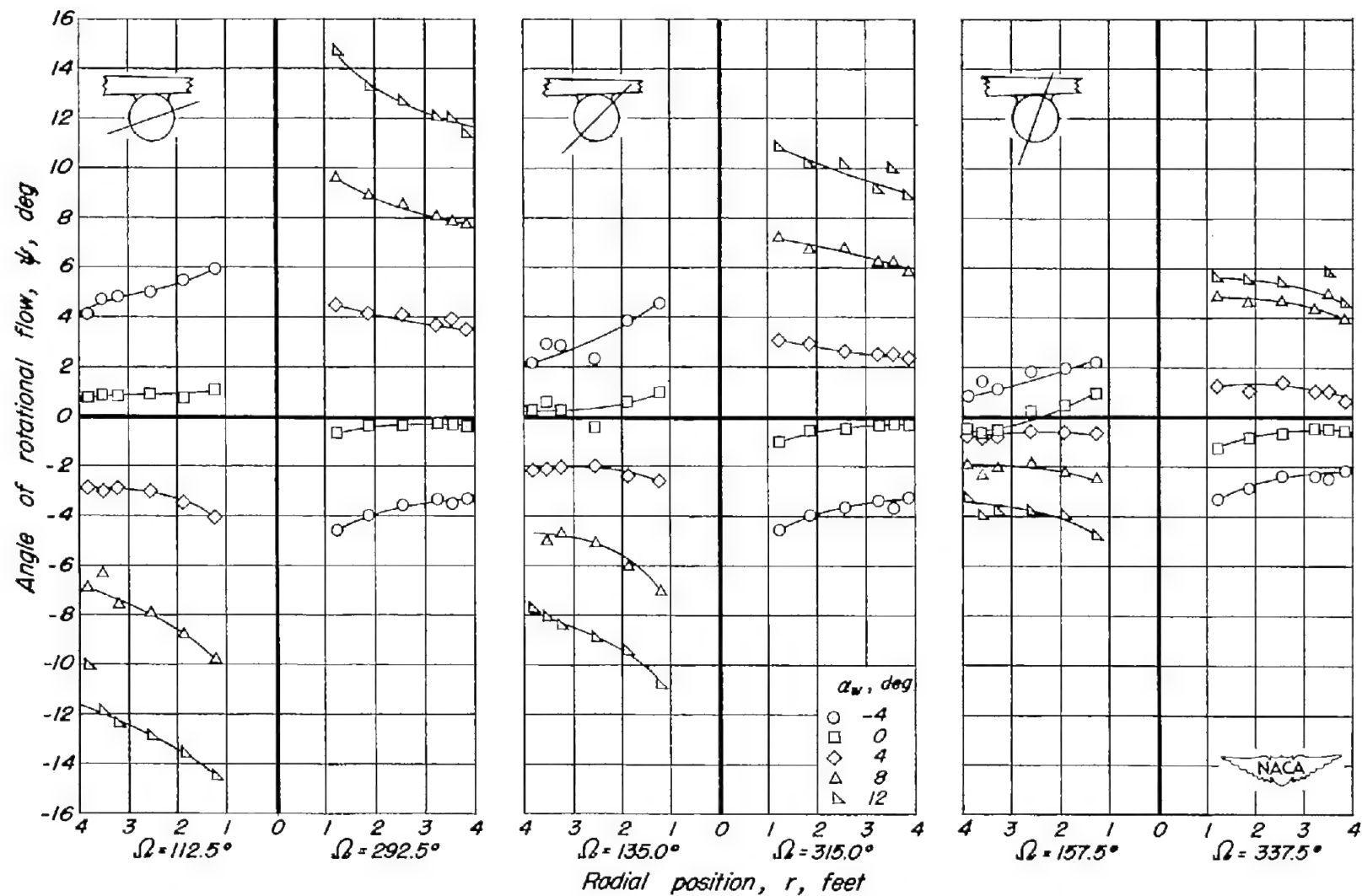


(a) $\Omega = 0^\circ, 22.5^\circ, 45.0^\circ, 180.0^\circ, 202.5^\circ, 225.0^\circ$

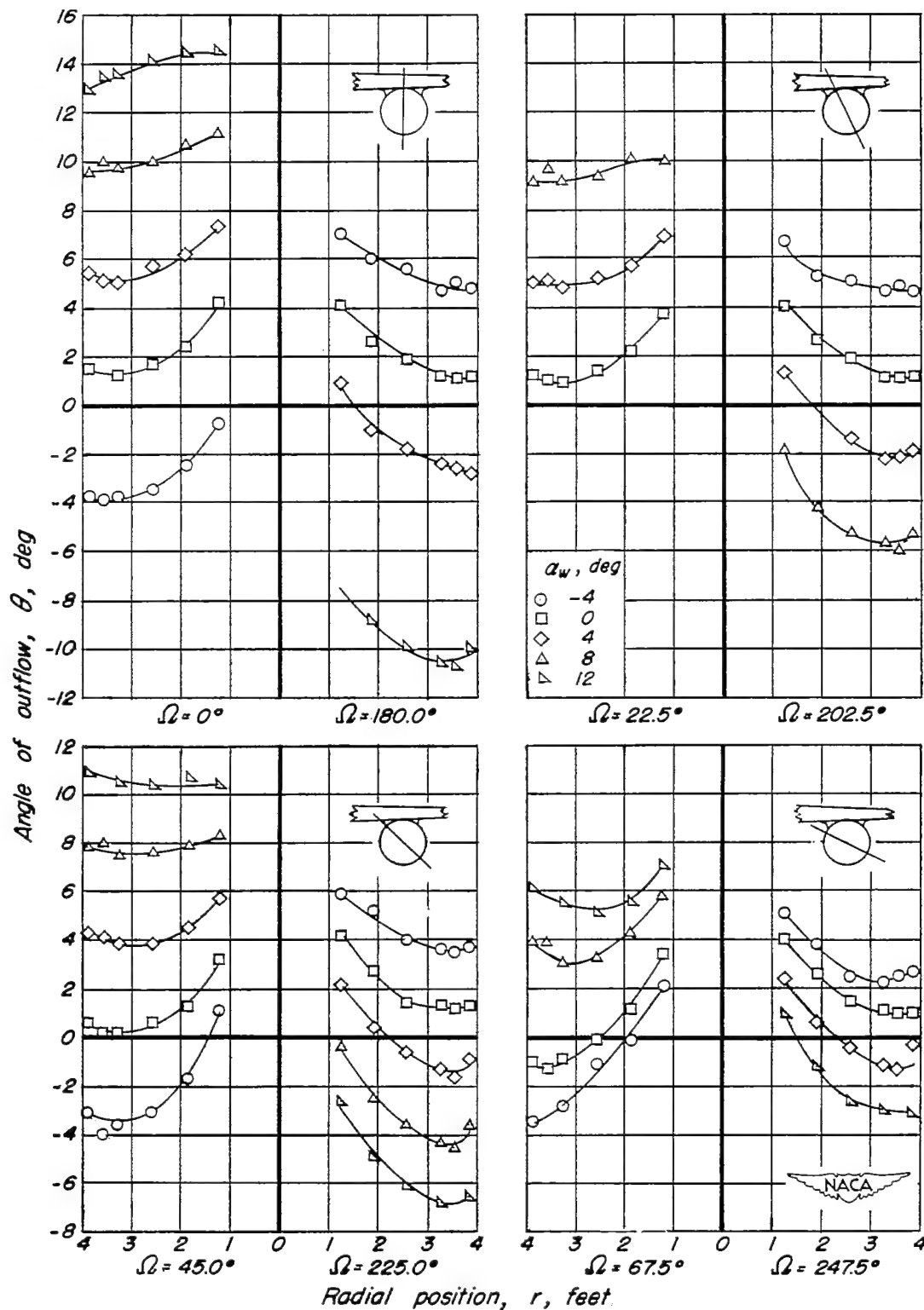
Figure 10. — Variation of the rotational flow angle ψ with radial position for several angles of attack. Inboard nacelle, Model B.



(b) $\Omega = 67.5^\circ, 90.0^\circ, 247.5^\circ, 270.0^\circ$
Figure 10. — Continued.

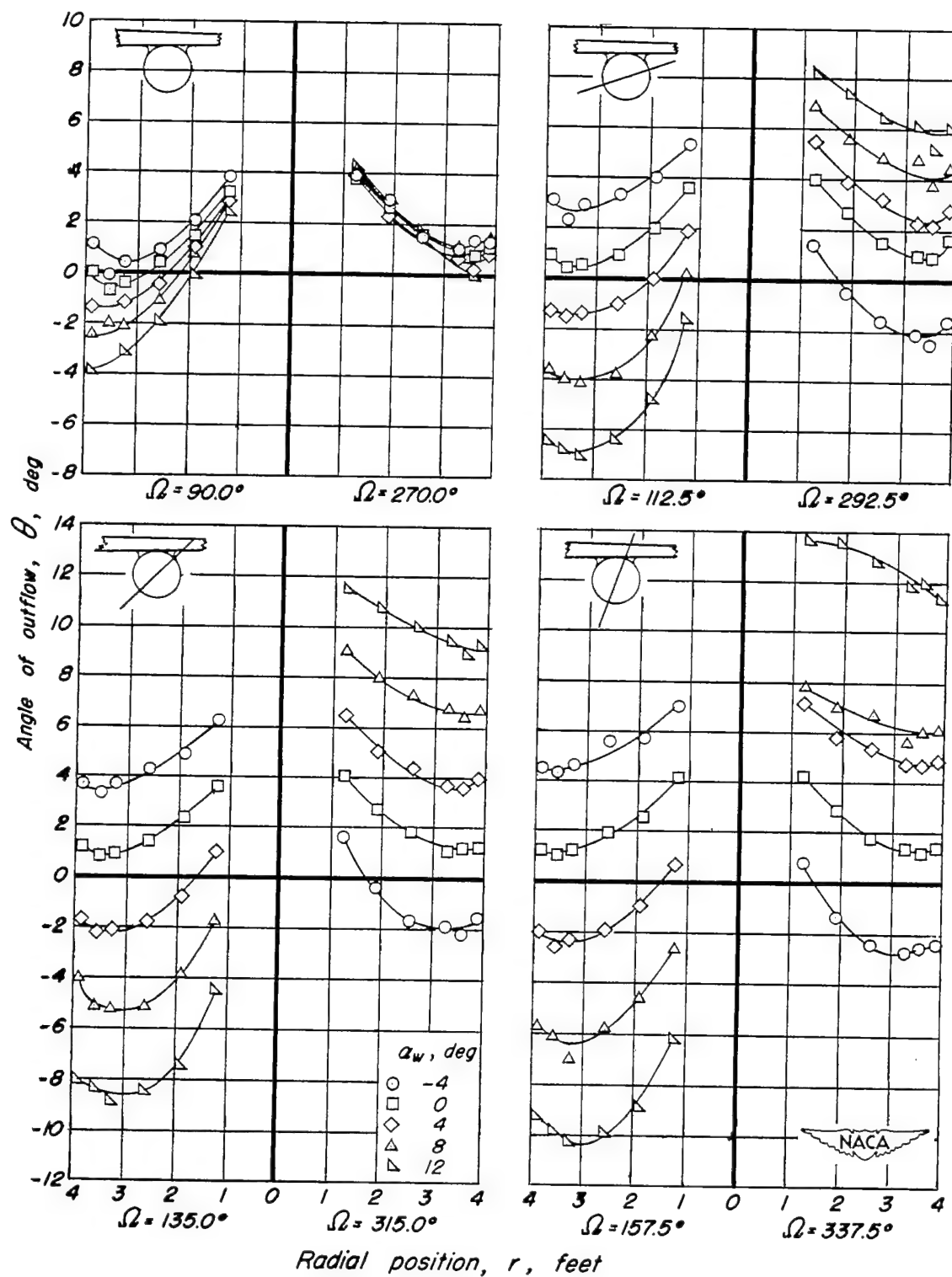


(c) $\Omega = 112.5^\circ, 135.0^\circ, 157.5^\circ, 292.5^\circ, 315.0^\circ, 337.5^\circ$
 Figure 10. — Concluded.



(a) $\Omega = 0^\circ, 22.5^\circ, 45.0^\circ, 67.5^\circ, 180^\circ, 202.5^\circ, 225.0^\circ, 247.5^\circ$

Figure 11.—Variation of the outflow angle θ with radial position for several angles of attack. Inboard nacelle, Model B.



(b) $\Omega = 90.0^\circ, 112.5^\circ, 135.0^\circ, 157.5^\circ, 270.0^\circ, 292.5^\circ, 315.0^\circ, 337.5^\circ$

Figure 11.— Concluded.

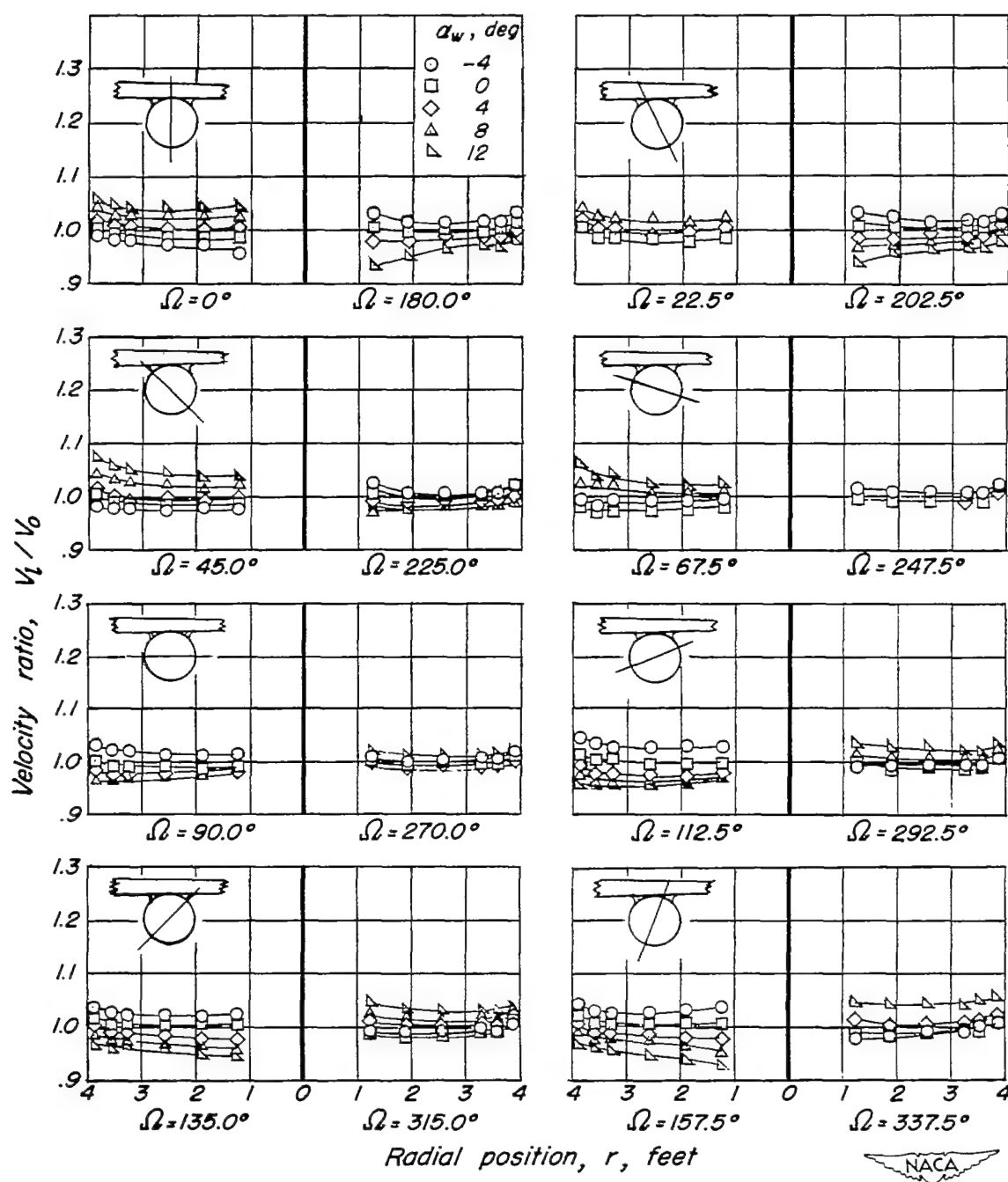
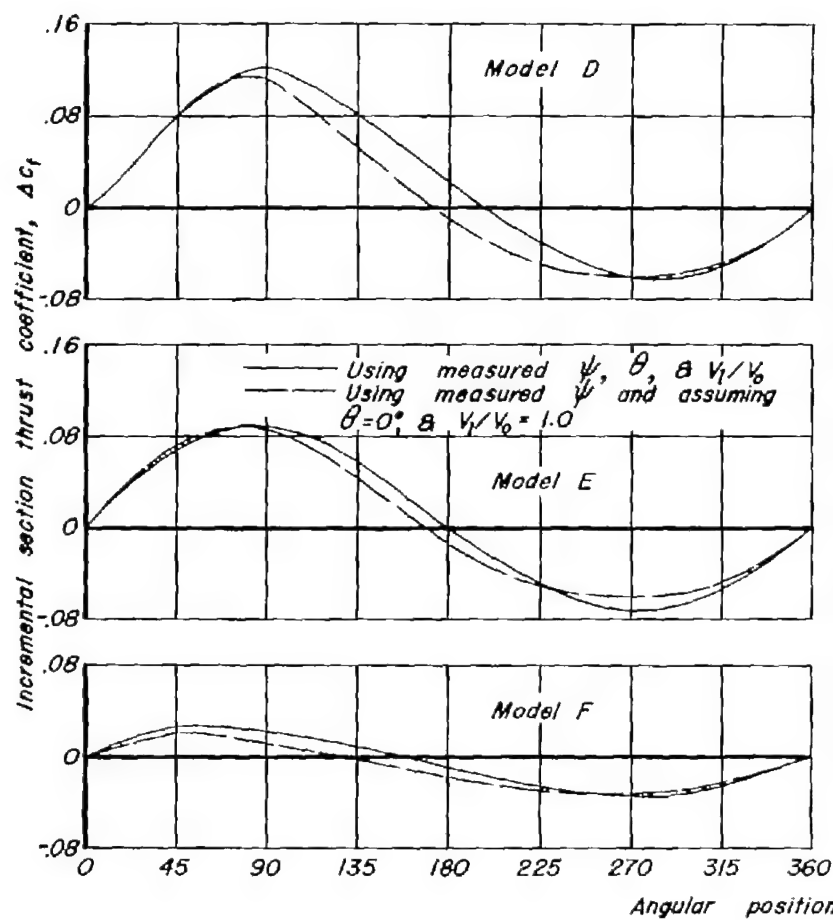
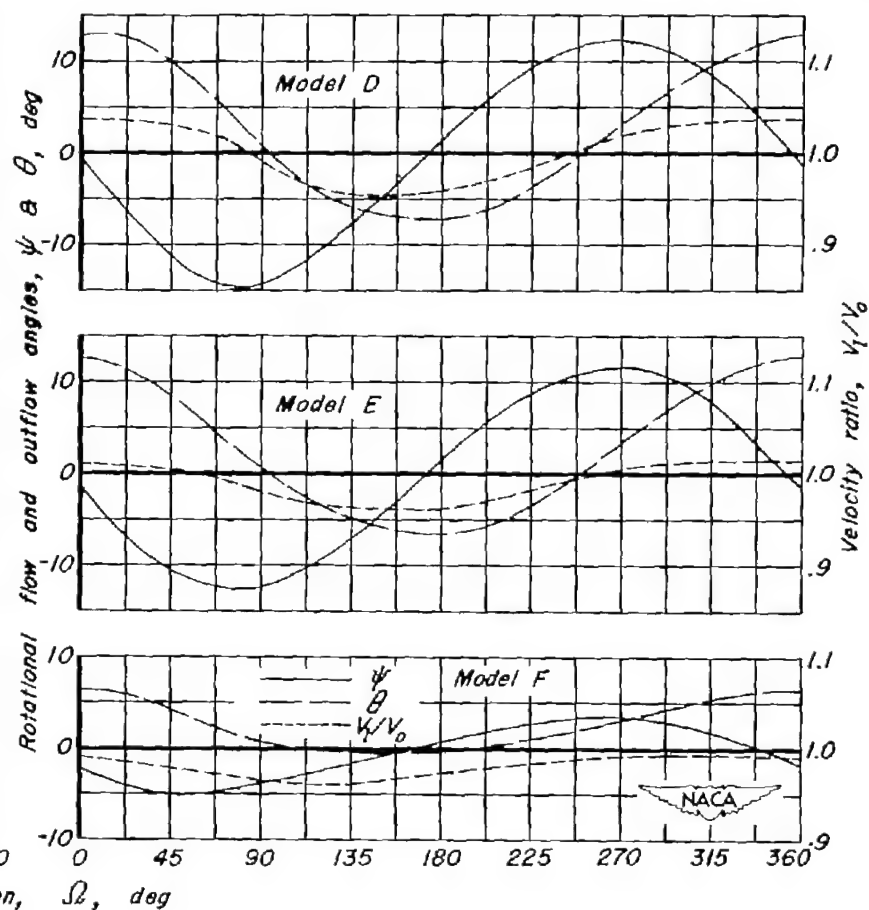


Figure 12.— Variation of the velocity ratio V_1/V_0 with radial position for several angles of attack. Inboard nacelle, model B.

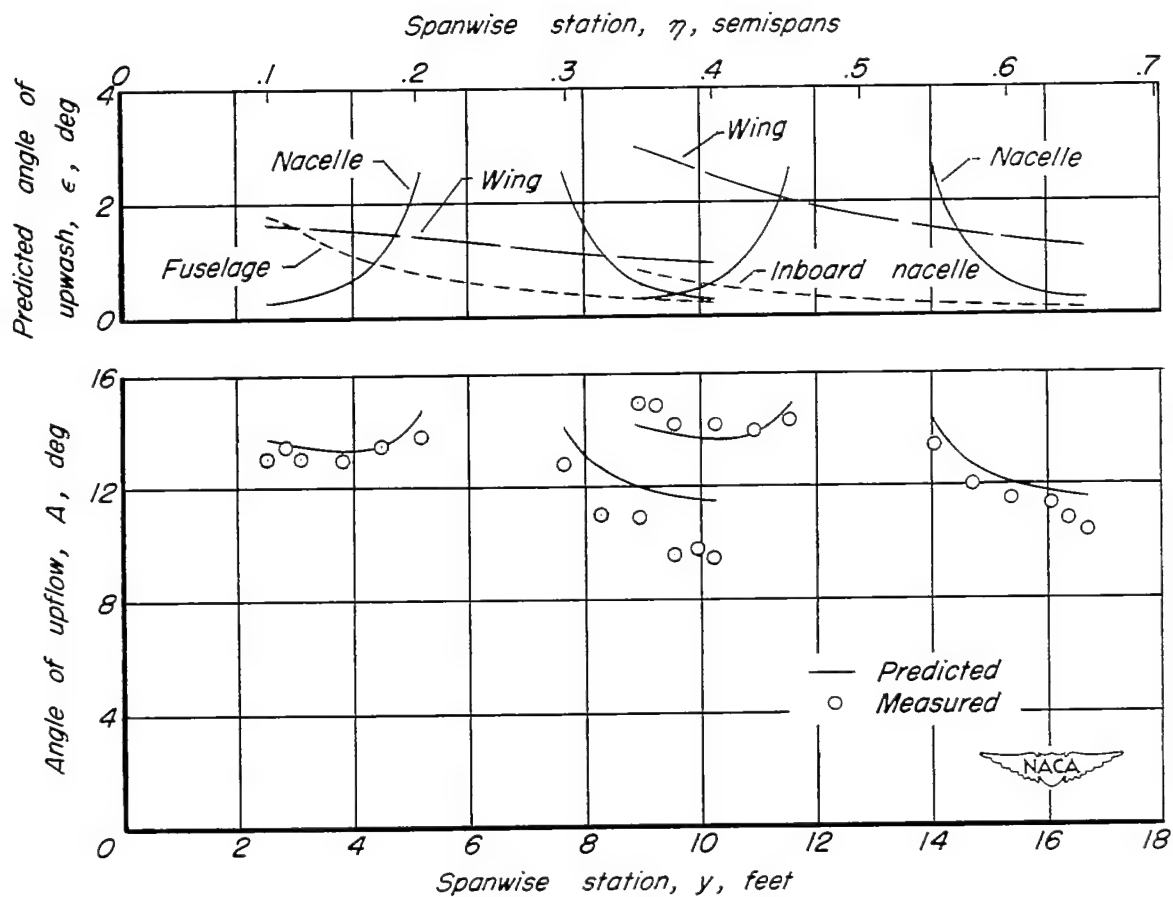
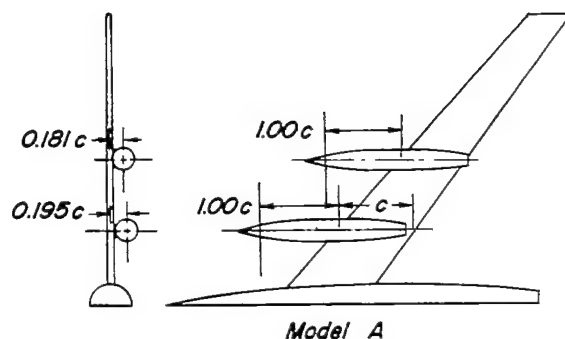


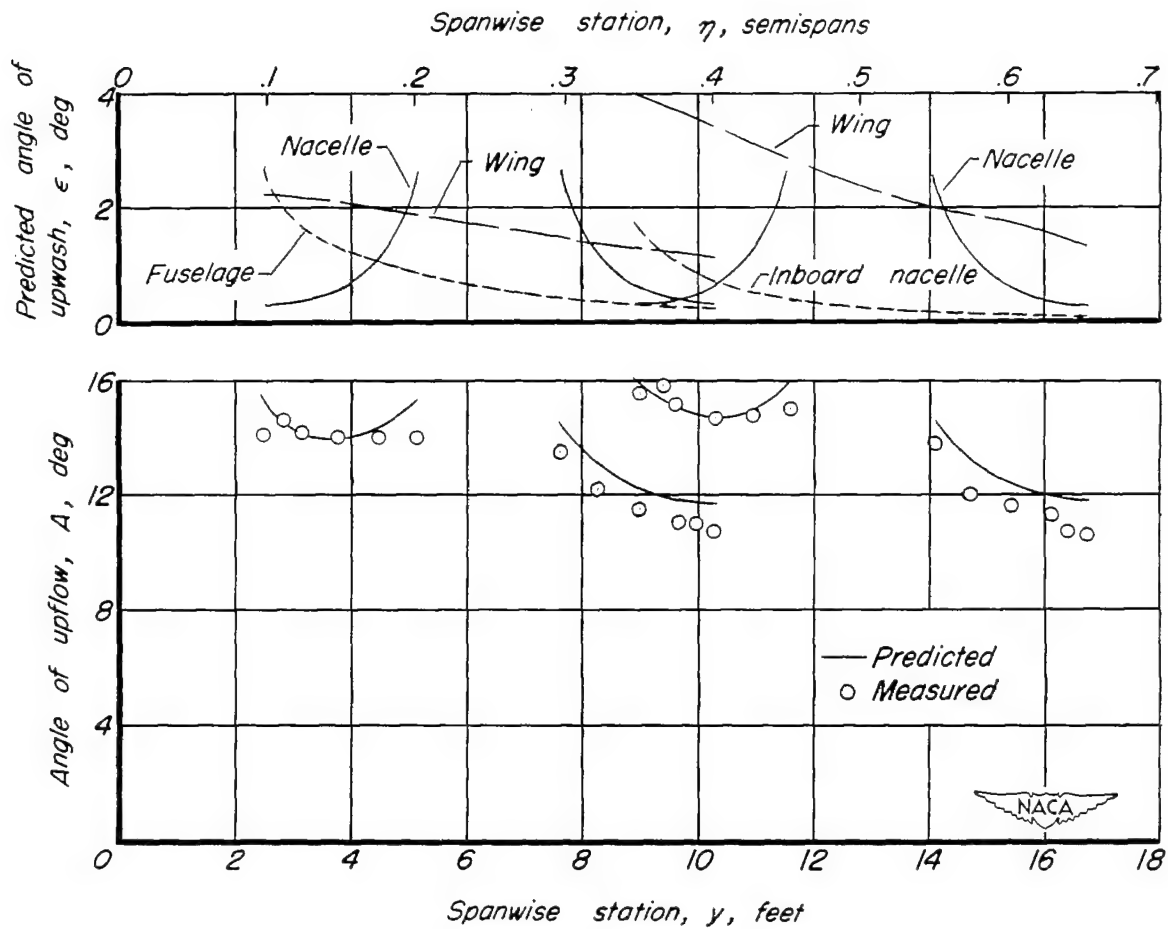
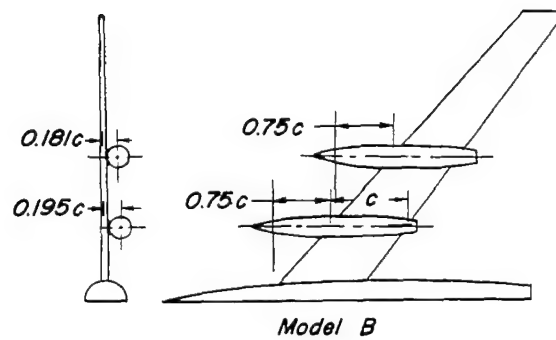
(a) Oscillating air loads.



(b) Flow-field parameters.

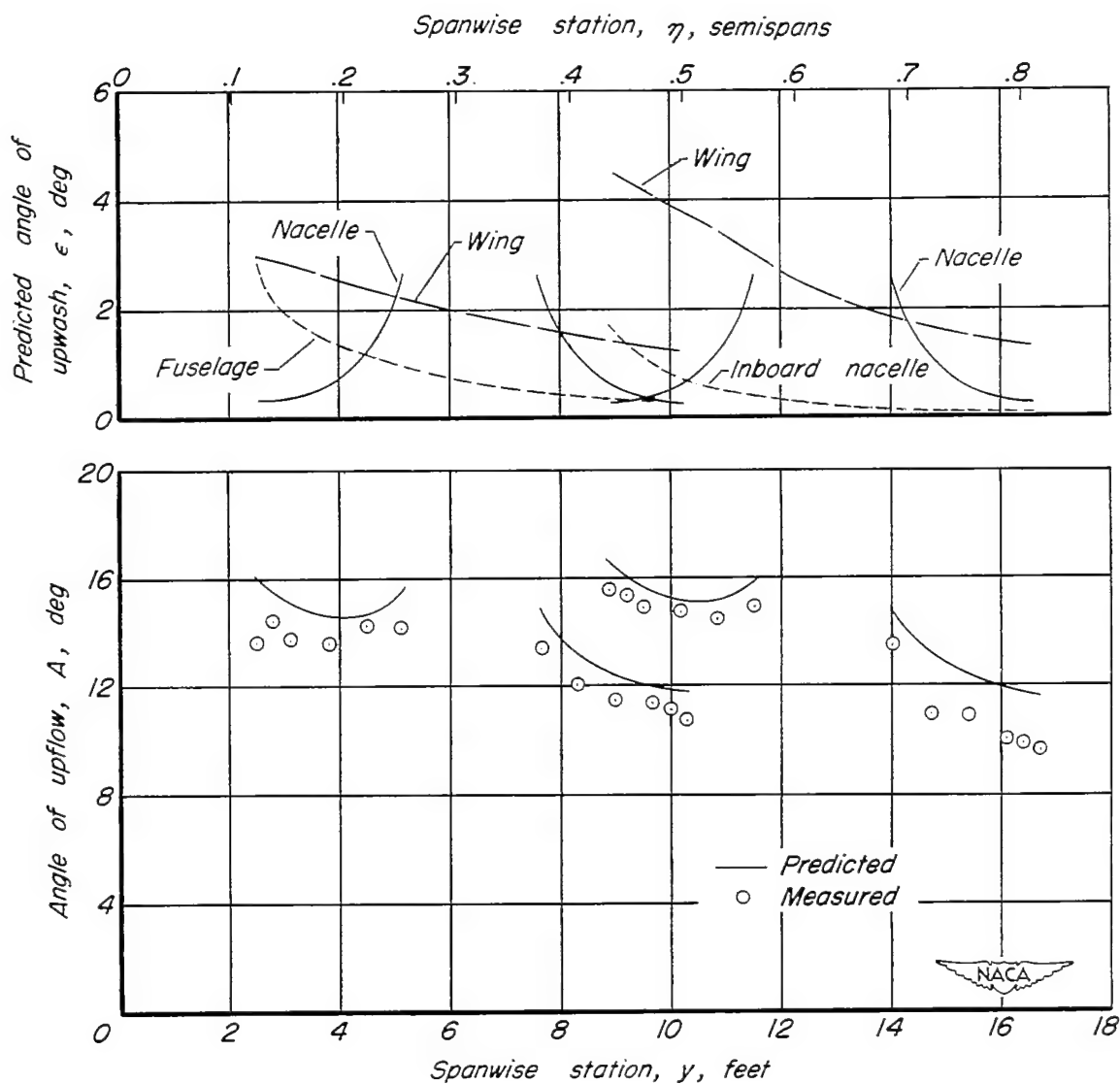
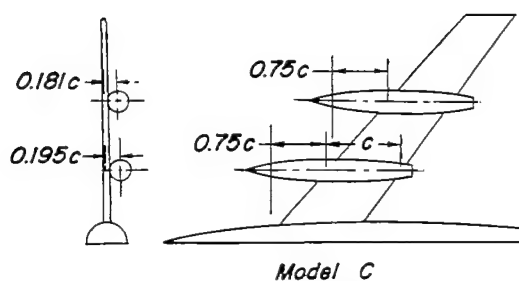
Figure 13.— Calculated oscillating air loads at the 0.75 station of a conventional propeller and associated measured flow-field data. $\alpha_w = 10^\circ$.

(a) Model A, $\alpha_G = 10^\circ$ Figure 14.— Measured and predicted upflow angles and predicted upwash components. $\alpha_W, 10^\circ$.



(b) Model B, $\alpha_G = 10^\circ$

Figure 14.— Continued.



(c) Model C, $\alpha_G = 10^\circ$

Figure 14. - Continued.

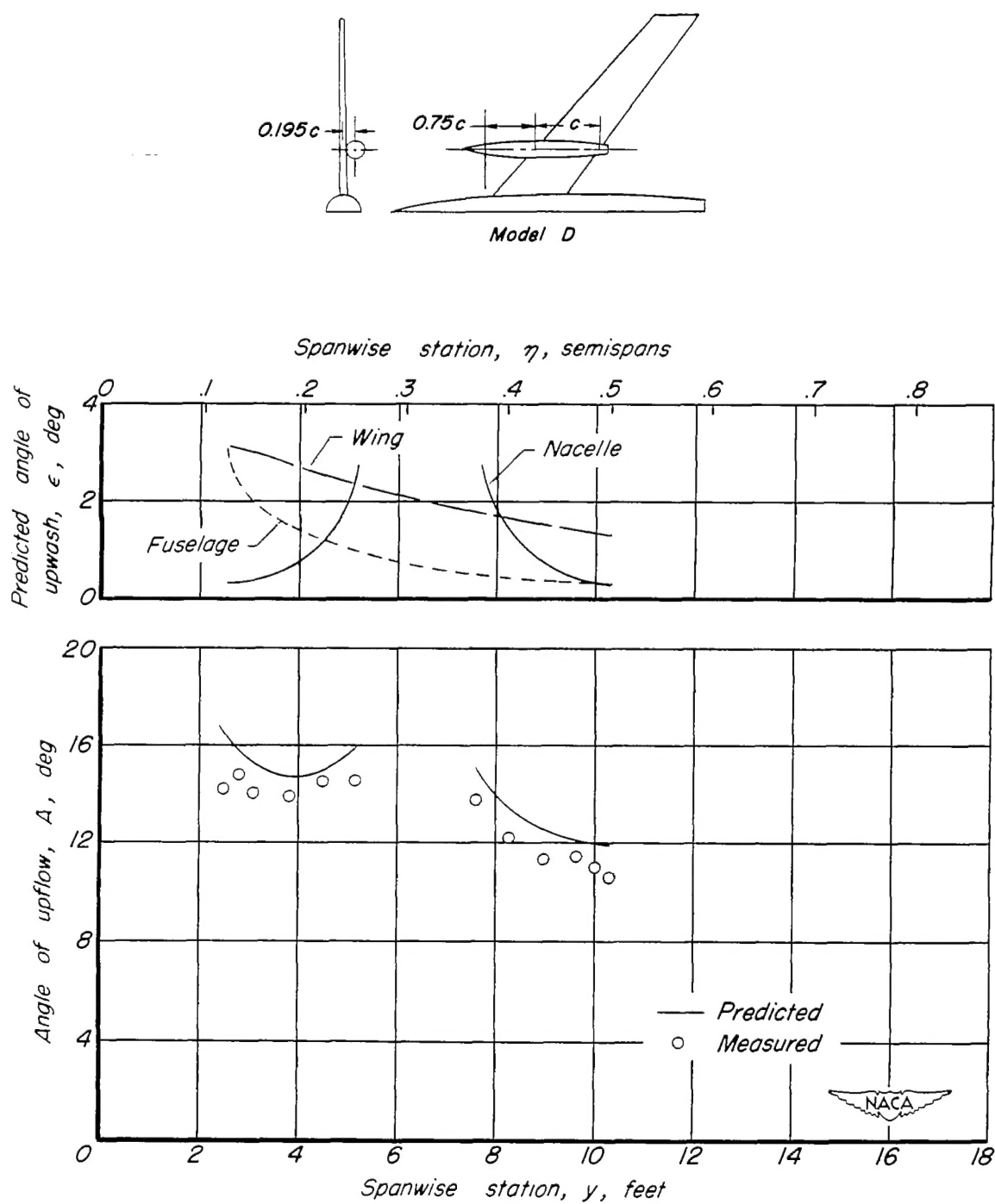
(d) Model D, $\alpha_6 = 10^\circ$

Figure 14. — Continued.

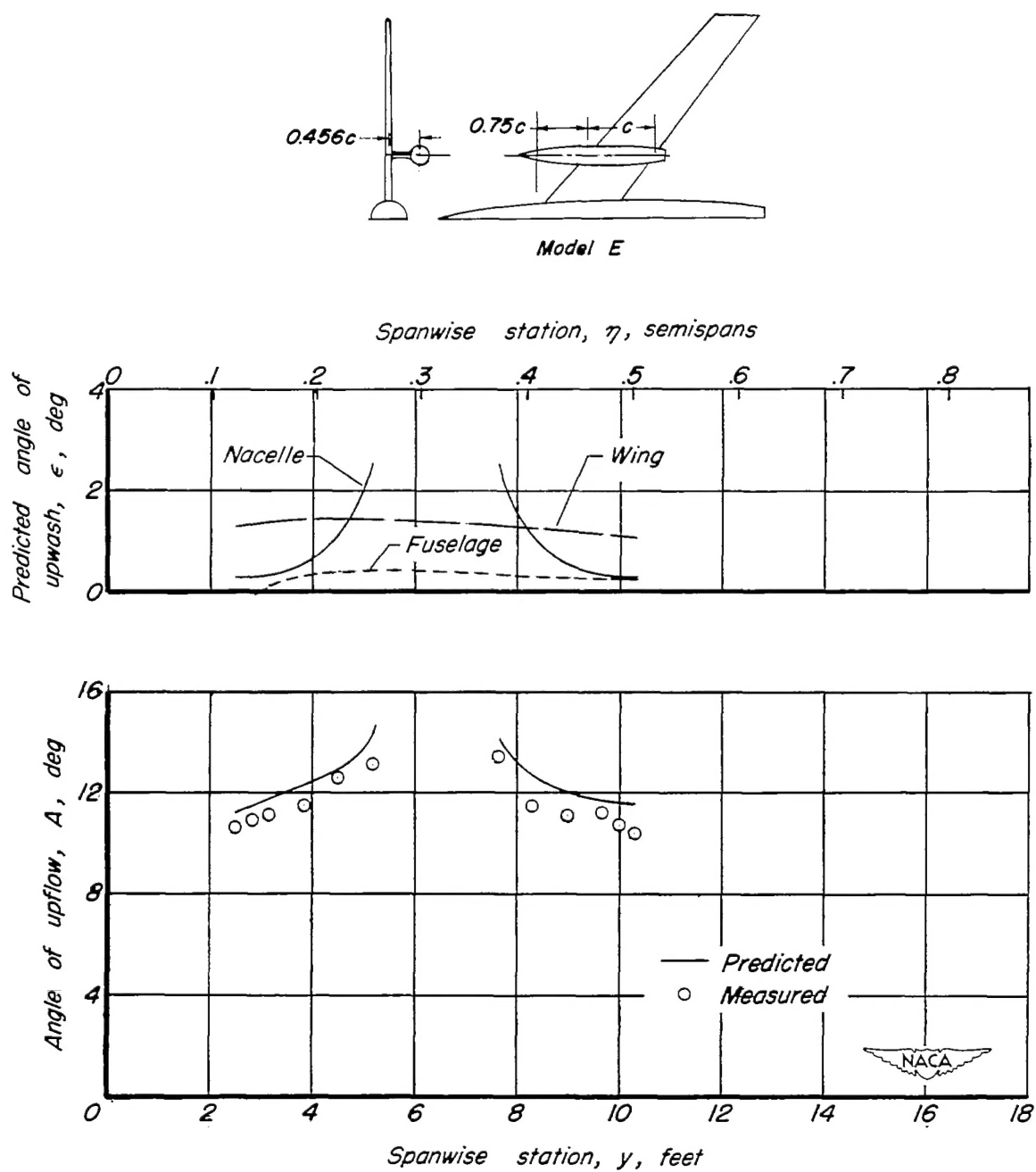
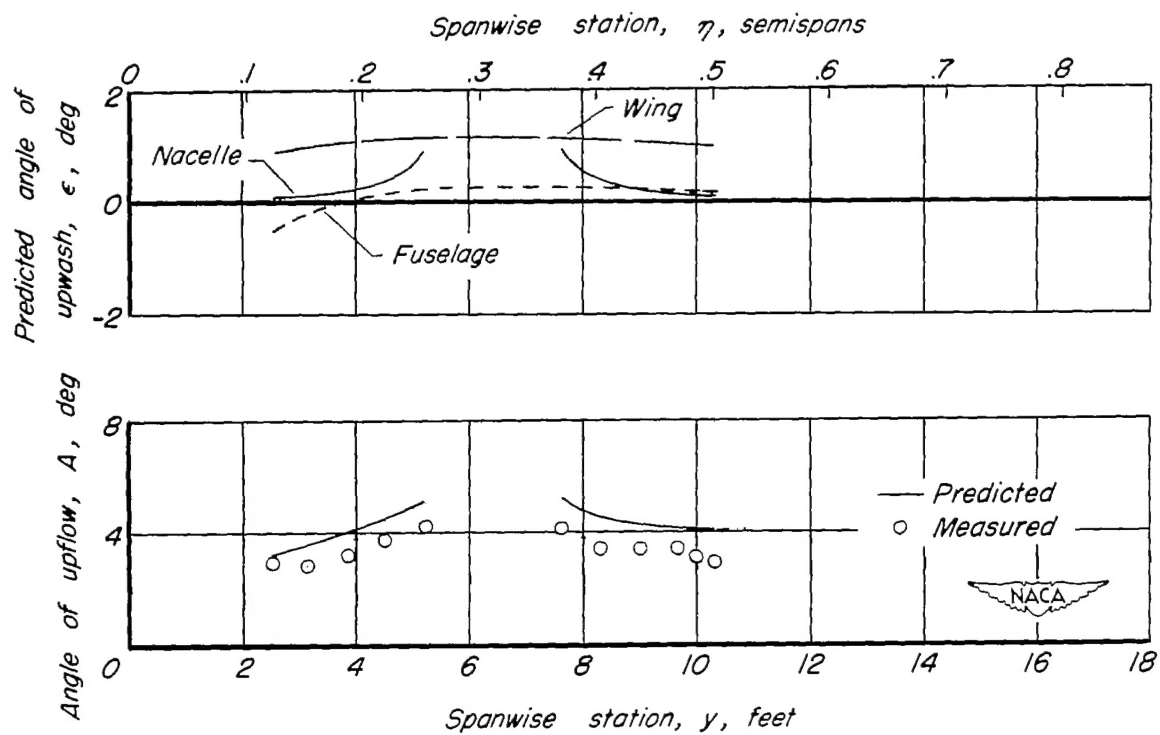
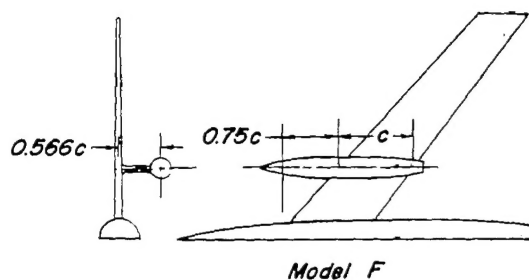
(e) Model E, $\alpha_0 = 10^\circ$

Figure 14.— Continued.



(f) Model F, $\alpha_6 = 3^\circ$

Figure 14.— Concluded.

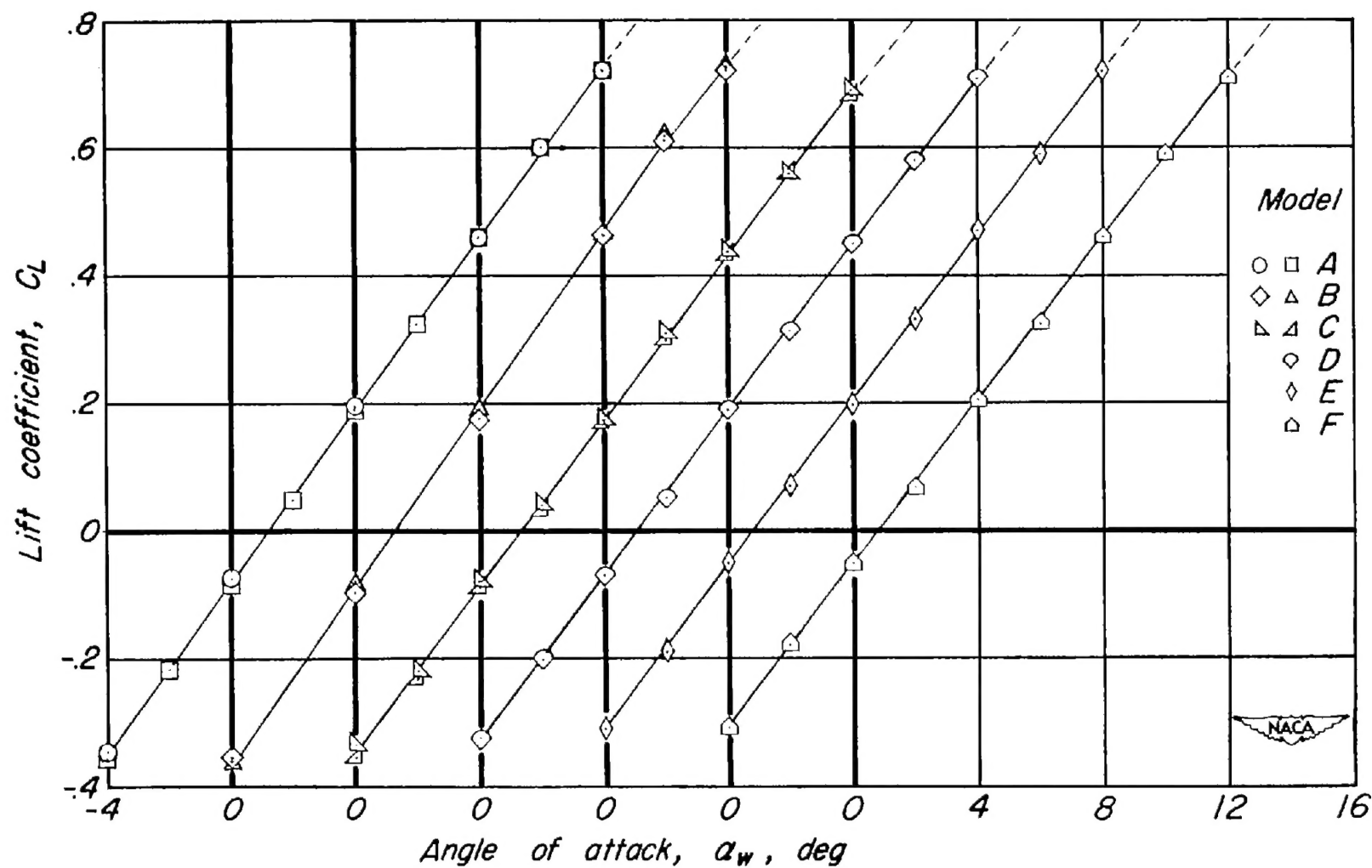


Figure 15. — Lift characteristics of semispan models. $\Lambda, 40^\circ$.